

Spin Dynamics in Hierarchical Black Hole Triples: Predicting Final Spin-Orbit Misalignment Angle From Initial Conditions

Yubo Su,¹ Dong Lai¹ Bin Liu¹

¹ *Cornell Center for Astrophysics and Planetary Science, Department of Astronomy, Cornell University, Ithaca, NY 14853, USA*

Accepted Jan 31, 2999. Received Jan 31, 2999; in original form Jan 31, 2999

ABSTRACT

Many previous studies have considered the spin and orbital dynamics of black hole (BH) binaries that undergo large eccentricity excitations through Lidov-Kozai oscillations due to the influence of a highly inclined tertiary companion and merge via gravitational wave radiation. However, these extreme eccentricity variations make such systems difficult to characterize analytically. In this paper, we provide an analytical formalism for understanding the spin dynamics of the inner BHs to quadrupole order. We show that, under certain conditions, the regular eccentricity oscillations of the binary can be averaged over to determine the long-term behavior of the system in a smooth and gradual way. In particular, we demonstrate that the final spin-orbit misalignment angle when the inner binary gravitationally decouples from the tertiary companion is often simply related to the binary’s primordial spin orientation through an approximate adiabatic invariant. We calculate the deviation from adiabaticity in closed form as a function of initial conditions. We also place accurate constraints on when this adiabatic invariant breaks down due to resonant interactions. We consider both stellar-mass and supermassive BH tertiary companions, and provide simple prescriptions for astrophysically relevant parameters.

Key words: black hole physics – gravitational waves – binaries: general – stars: kinematics and dynamics

1 INTRODUCTION

As LIGO/VIRGO continues to detect mergers of black hole (BH) binaries (e.g. Abbott et al. 2016, 2019), it is increasingly important to systematically study various formation channels of BH binaries and their observable signatures. The canonical channel consists of isolated binary evolution, in which mass transfer and friction in the common envelope phase cause the binary orbit to decay sufficiently that it subsequently merges via emission of gravitational waves (GW) within a Hubble time (e.g. Lipunov et al. 1997, 2017; Podsiadlowski et al. 2003; Belczynski et al. 2010, 2016; Dominik et al. 2012, 2013, 2015). BH binaries formed via isolated binary evolution are generally expected to have small misalignment between the BH spin axis and the orbital angular momentum axis (Postnov & Kuranov 2019; Belczynski et al. 2020). On the other hand, various flavors of dynamical formation channels of BH binaries have also been studied. These involve either strong gravitational scatterings in dense clusters (e.g. Zwart & McMillan 1999; O’leary et al. 2006; Miller & Lauburg 2009; Banerjee et al. 2010; Downing et al. 2010; Ziosi et al. 2014; Rodriguez et al. 2015; Samsing & Ramirez-Ruiz 2017; Samsing & D’Orazio 2018; Rodriguez et al. 2018; Gondán et al. 2018) or more gentle “tertiary-induced mergers” (e.g. Blaes et al. 2002; Miller & Hamilton 2002; Wen 2003; Antonini & Perets 2012; Antonini et al. 2017; Silsbee & Tremaine 2016; Liu & Lai 2017, 2018; Randall & Xianyu 2018; Hoang et al. 2018). The dy-

namical formation channels generally produce BH binaries with misaligned spins.

GW observations of binary inspirals can put constraints on BH masses and spins. Typically, spin constraints come in the form of two dimensionless mass-weighted combinations of the component BH spins: (i) the aligned spin parameter

$$\chi_{\text{eff}} \equiv \frac{m_1 \chi_1 \cos \theta_{s1l} + m_2 \chi_2 \cos \theta_{s2l}}{m_1 + m_2}, \quad (1)$$

where $m_{1,2}$ are the masses of the BHs, θ_{s1l} is the angle between the i th spin and the binary orbital angular momentum axis, and $\chi_i \equiv cS_i/(Gm_i^2)$ is the dimensionless Kerr spin parameter; and (ii) the perpendicular spin parameter (Schmidt et al. 2015)

$$\chi_p \equiv \max \left\{ \chi_1 \sin \theta_{s1l}, \frac{q(4q+3)}{4+3q} \chi_2 \sin \theta_{s2l} \right\}, \quad (2)$$

where $q \equiv m_2/m_1$. The systems detected in the O1 and O2 observing runs have small χ_{eff} , which is consistent with either small χ_1 and χ_2 or highly misaligned BH spins ($\theta_{s1l} \approx 90^\circ$). The recently-announced LIGO detection GW190521 (Abbott et al. 2020) has $\chi_{\text{eff}} = 0.08^{+0.27}_{-0.38}$ while $\chi_p = 0.68^{+0.25}_{-0.37}$. The spin-orbit misalignment angles of the two merging BHs are reported to be 81^{+64}_{-53} and 85^{+57}_{-55} degrees respectively.

Liu & Lai (2017, 2018 hereafter LL17, LL18), and Liu et al. (2019) carried out a systematic study of binary BH mergers in the

presence of a tertiary companion. LL17 pointed out the important effect of spin-orbit coupling (de-Sitter precession) in determining the final spin-orbit misalignment angles of BH binaries in triple systems. They considered binaries with sufficiently compact orbits (so that mergers are possible even without a tertiary) and showed that the combination of LK oscillations (induced by a modestly inclined tertiary) and spin-orbit coupling gives rise to a broad range of final spin-orbit misalignment in the merging binary BHs. We call these mergers *LK-enhanced mergers*. LL18 considered the most interesting case of *LK-induced mergers*, in which an initially wide BH binary (too wide to merge in isolation) is pushed to extreme eccentricities (close to unity) by a highly inclined tertiary and merges within a few Gyrs. LL18 examined a wide range of orbital and spin evolution behaviors and found that LK-induced mergers can sometimes yield a “90° attractor”: when the BH spin is initially aligned with the inner binary angular momentum axis ($\theta_{\text{sl},0} = 0$), it evolves towards a perpendicular state ($\theta_{\text{sl},f} = 90^\circ$) near merger. Qualitatively, they found that the attractor exists when the LK-induced orbital decay is sufficiently “gentle” and the octupole effect is unimportant. Fig. 1 gives an example of a system evolving towards this attractor, where θ_{sl} converges to $\approx 90^\circ$ at late times in the bottom right panel. Fig. 2 shows how $\theta_{\text{sl},f}$ varies when the initial inclination of the tertiary orbit I_0 (relative to the inner orbit) is varied. Note that for rapid mergers (when I_0 is close to 90°), the attractor does not exist; as I_0 deviates more from 90° , the merger time increases and $\theta_{\text{sl},f}$ is close to 90° . This 90° attractor gives rise to a peak around $\chi_{\text{eff}} = 0$ in the final χ_{eff} distribution in tertiary-induced mergers (LL18; Liu et al. 2019). This peak was also found in the population studies of Antonini et al. (2018).

The physical origin of this 90° attractor and under what conditions it can be achieved are not well understood. LL18 proposed an explanation based on analogy with an adiabatic invariant in systems where the inner binary remains circular throughout the inspiral (LL17). However, this analogy is not justified, as significant eccentricity excitation is a necessary ingredient in LK-induced mergers. In addition, the LK-enhanced mergers considered in LL17 show no 90° attractor even though the orbital evolution is slow and regular.

In this paper, we study an analytic theory that reproduces the 90° attractor and characterizes its regime of validity. In Sections 2 and 3, we set up the relevant equations of motion for the orbital and spin evolution of the system. In Sections 4 and 5, we develop an analytic understanding of the spin evolution. In Section 6, we generalize our results to stellar-mass tertiary companions. We discuss and conclude in Section 7.

2 LK-INDUCED MERGERS: ORBITAL EVOLUTION

In this section we summarize the key features and relevant equations for LK-induced mergers to be used for our analysis in later sections. Consider a black hole (BH) binary with masses m_1 and m_2 having total mass m_{12} , reduced mass $\mu = m_1 m_2 / m_{12}$, semi-major axis a and eccentricity e . This inner binary orbits around a tertiary with mass m_3 , semimajor axis a_{out} and eccentricity e_{out} in a hierarchical configuration ($a_{\text{out}} \gg a$). Unless explicitly stated, we assume $m_3 \gg m_1, m_2$ (so the tertiary is a supermassive black hole, or SMBH), although our analysis can be easily generalized to comparable masses. We denote the orbital angular momentum of the inner binary by $\mathbf{L} \equiv L\hat{\mathbf{L}}$ and the angular momentum of the outer binary by $\mathbf{L}_{\text{out}} \equiv L_{\text{out}}\hat{\mathbf{L}}_{\text{out}}$. Since $L_{\text{out}} \gg L$, we take \mathbf{L}_{out} to be fixed.

The equations of motion governing the orbital elements a , e ,

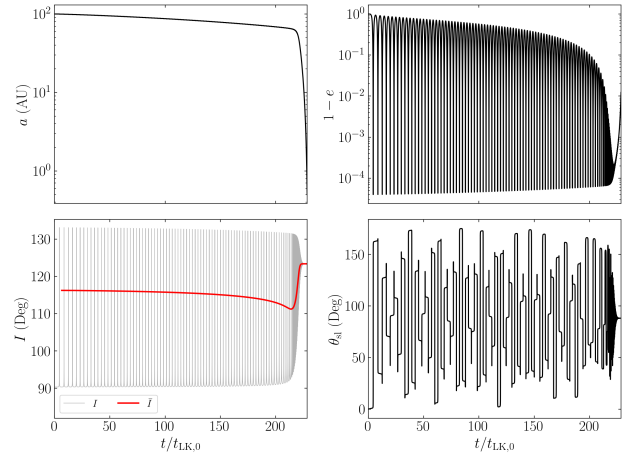


Figure 1. An example of the 90° spin attractor in LK-induced BH binary mergers. The four panes show the time evolution of the binary semi-major axis a , eccentricity e , inclination I [the red line denotes the averaged \bar{I} given by Eq. (28)], and spin-orbit misalignment angle θ_{sl} . The unit of time $t_{\text{LK},0}$ is the LK timescale [Eq. (9)] evaluated for the initial conditions. The inner binary has $m_1 = 30M_\odot$, $m_2 = 20M_\odot$, and initial $a_0 = 100$ AU, $e_0 = 0.001$, $I_0 = 90.35^\circ$ (with respect to the outer binary), and $\theta_{\text{sl},0} = 0$. The tertiary SMBH has $a_{\text{out}} = 2.2$ pc, $e_{\text{out}} = 0$, and $m_3 = 3 \times 10^7 M_\odot$. It can be seen that θ_{sl} evolves to $\sim 90^\circ$ as a decays to smaller values, and we stop the simulation when $a = 0.5$ AU as θ_{sl} has converged.

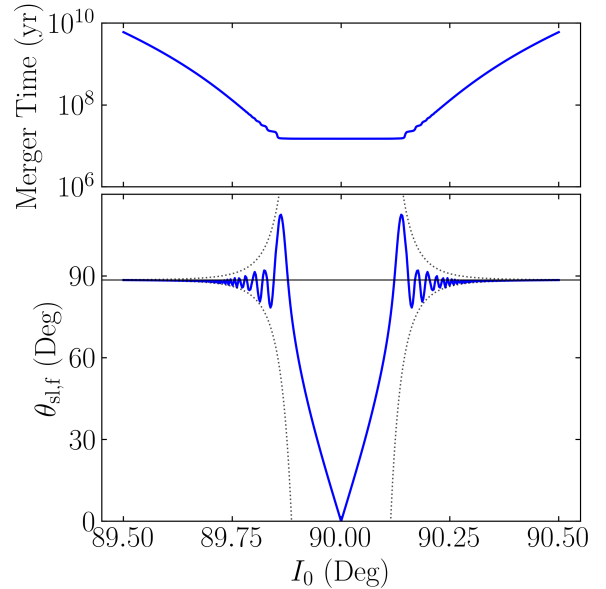


Figure 2. The merger time and the final spin-orbit misalignment angle $\theta_{\text{sl},f}$ as a function of the initial inclination I_0 for LK-induced mergers. The other parameters are the same as those in Fig. 1. For I_0 somewhat far away from 90° , the resulting $\theta_{\text{sl},f}$ are all quite near 90° . The horizontal black solid line shows the predicted $\theta_{\text{sl},f}$ if $\bar{\theta}_e$ is conserved, i.e. Eq. (56). The black dashed line in the lower panel shows Eq. (60), which provides an estimate for the deviation from the 90° attractor.

$\delta\Omega$, I , ω (where $\delta\Omega$, I , ω are the longitude of the ascending node, inclination, and argument of periapsis respectively) of the inner binary are

$$\frac{da}{dt} = \left(\frac{da}{dt}\right)_{\text{GW}}, \quad (3)$$

$$\frac{de}{dt} = \frac{15}{8t_{\text{LK}}} e j(e) \sin 2\omega \sin^2 I + \left(\frac{de}{dt}\right)_{\text{GW}}, \quad (4)$$

$$\frac{d\delta\Omega}{dt} = \frac{3}{4t_{\text{LK}}} \frac{\cos I (5e^2 \cos^2 \omega - 4e^2 - 1)}{j(e)}, \quad (5)$$

$$\frac{dI}{dt} = -\frac{15}{16t_{\text{LK}}} \frac{e^2 \sin 2\omega \sin 2I}{j(e)}, \quad (6)$$

$$\frac{d\omega}{dt} = \frac{3}{4t_{\text{LK}}} \frac{2j^2(e) + 5 \sin^2 \omega (e^2 - \sin^2 I)}{j(e)} + \Omega_{\text{GR}}, \quad (7)$$

where we have defined

$$j(e) = \sqrt{1 - e^2}, \quad (8)$$

$$t_{\text{LK}}^{-1} \equiv n \left(\frac{m_3}{m_{12}}\right) \left(\frac{a}{\tilde{a}_{\text{out}}}\right)^3, \quad (9)$$

with $n \equiv \sqrt{Gm_{12}/a^3}$ the mean motion of the inner binary, and $\tilde{a}_{\text{out}} = a_{\text{out}} \sqrt{1 - e_{\text{out}}^2}$. The GR-induced apsidal precession of the inner binary is given by

$$\Omega_{\text{GR}}(e) = \frac{3Gnm_{12}}{c^2 a j^2(e)}. \quad (10)$$

The dissipative terms due to gravitational radiation are

$$\left(\frac{da}{dt}\right)_{\text{GW}} = -\frac{a}{t_{\text{GW}}(e)}, \quad (11)$$

$$\left(\frac{de}{dt}\right)_{\text{GW}} = -\frac{304}{15} \frac{G^3 \mu m_{12}^2}{c^5 a^4} \frac{1}{j^{5/2}(e)} \left(1 + \frac{121}{304} e^2\right), \quad (12)$$

where

$$t_{\text{GW}}^{-1}(e) \equiv \frac{64}{5} \frac{G^3 \mu m_{12}^2}{c^5 a^4} \frac{1}{j^{7/2}(e)} \left(1 + \frac{73}{24} e^2 + \frac{37}{96} e^4\right). \quad (13)$$

In Fig. 1, we provide an example of an LK-induced merger for our fiducial parameters (described in the figure caption). In this example, the inner binary initially coalesces slowly as regular LK oscillations excite the eccentricity to a consistent maximum near unity. Then, as a decreases and the minimum eccentricity within each LK cycle increases, the orbital decay of the inner binary accelerates. Once the binary becomes sufficiently compact, the spin-orbit precession timescale is very short, and θ_{sl} reaches a constant value $\approx 90^\circ$. At the same time, apsidal precession suppresses further eccentricity oscillations, and the eccentricity begins to rapidly decay to 0. We terminate the simulation at $a = 0.5$ AU as θ_{sl} has reached its final value, even though the system still has substantially nonzero eccentricity. Since $\tilde{a}_{\text{out}} \gg a$, the octupole effects are negligible and have been omitted in Eqs. (4–7). Note that these parameters give the same t_{LK} as Fig. 4 of LL18. We refer to this as the fiducial parameter regime, and our analysis in later sections will be based on this example unless otherwise noted.

We next discuss the key analytical properties of the orbital evolution.

2.1 Analytical Results Without GW Radiation

First, neglecting the GW radiation terms, the system admits two conservation laws, the “Kozai constant” and energy conservation,

$$j(e) \cos I = \text{const}, \quad (14)$$

$$\frac{3}{8} \left[2e^2 + j^2(e) \cos^2 I - 5e^2 \sin^2 I \sin^2 \omega \right] + \frac{\epsilon_{\text{GR}}}{j(e)} = \text{const}, \quad (15)$$

(see Anderson et al. 2016, LL18 for more general expressions when L_{out} is comparable to L), where

$$\epsilon_{\text{GR}} \equiv (\Omega_{\text{GR}} t_{\text{LK}})_{e=0} = \frac{3Gm_{12}^2 \tilde{a}_{\text{out}}^3}{c^2 m_3 a^4}. \quad (16)$$

The conservation laws can be combined to obtain the maximum eccentricity e_{max} as a function of the initial I_0 (and initial $e_0 \ll 1$). The largest value of e_{max} occurs at $I_0 = 90^\circ$ and is given by

$$j(e_{\text{max}})_{I_0=90^\circ} = (8/9)\epsilon_{\text{GR}}. \quad (17)$$

Eccentricity excitation then requires $\epsilon_{\text{GR}} < 9/8$. Our fiducial examples in Figs. 1 and 2 satisfy $\epsilon_{\text{GR}} \ll 1$ at $a = a_0$, leading to $e_{\text{max}} \sim 1$ within a narrow inclination window around $I_0 = 90^\circ$.

Eqs. (14) and (15) imply that e is a function of $\sin^2 \omega$ alone (see Kinoshita 1993; Storch & Lai 2015 for exact forms), so an eccentricity maximum occurs every half period of ω . We define the period and angular frequency of eccentricity oscillation via

$$\pi = \int_0^{P_{\text{LK}}} \frac{d\omega}{dt} dt, \quad \Omega_{\text{LK}} \equiv \frac{2\pi}{P_{\text{LK}}}. \quad (18)$$

In LK cycles, the inner binary oscillates between the eccentricity minimum e_{min} and maximum e_{max} . The oscillation is “uneven”: when $e_{\text{min}} \ll e_{\text{max}}$, the binary spends a fraction $\sim j(e_{\text{max}})$ of the LK cycle, or time $\Delta t \sim t_{\text{LK}} j(e_{\text{max}})$, near $e \approx e_{\text{max}}$ [see Eq. (7)].

2.2 Behavior with GW Radiation

Including the effect of GW radiation, orbital decay predominantly occurs at $e \approx e_{\text{max}}$ with the timescale of $t_{\text{GW}}(e_{\text{max}})$ [see Eq. (13)]. On the other hand, Eq. (7) implies that, when $\epsilon_{\text{GR}} \ll 1$, the binary spends only a small fraction ($\sim j(e_{\text{max}})$) of the time near $e \approx e_{\text{max}}$. Thus, we expect two qualitatively different merger behaviors:

- “Rapid mergers”: When $t_{\text{GW}}(e_{\text{max}}) \lesssim t_{\text{LK}} j(e_{\text{max}})$, the binary is “pushed” into high eccentricity and exhibits a “one shot merger” without any e -oscillations.
- “Smooth mergers”: When $t_{\text{GW}}(e_{\text{max}}) \gtrsim t_{\text{LK}} j(e_{\text{max}})$, the binary goes through a phase of eccentricity oscillations while the orbit gradually decays. In this case, the LK-averaged orbital decay rate is $\sim j(e_{\text{max}}) t_{\text{GW}}^{-1}(e_{\text{max}})$. As a decreases, e_{max} decreases slightly while the minimum eccentricity increases, approaching e_{max} (see Fig. 1). This eccentricity oscillation “freeze” ($e_{\text{min}} \sim e_{\text{max}}$) is due to GR-induced apsidal precession (ϵ_{GR} increases as a decreases), and occurs when $\epsilon_{\text{GR}}(a) \gg j(e_{\text{max}})$. After the eccentricity is frozen, the binary circularizes and decays on the timescale $t_{\text{GW}}(e_{\text{max}})$.

3 SPIN DYNAMICS: EQUATIONS

We are interested in the spin orientations of the inner BHs at merger as a function of initial conditions. Since they evolve independently to leading post-Newtonian order, we focus on the dynamics of $\hat{\mathbf{S}}_1 = \hat{\mathbf{S}}$, the spin vector of m_1 . Since the spin magnitude does not enter into

the dynamics, we write $\mathbf{S} \equiv \hat{\mathbf{S}}$ for brevity (i.e. \mathbf{S} is a unit vector). Neglecting spin-spin interactions, \mathbf{S} undergoes de Sitter precession about \mathbf{L} as

$$\frac{d\mathbf{S}}{dt} = \Omega_{\text{SL}} \hat{\mathbf{L}} \times \mathbf{S}, \quad (19)$$

with

$$\Omega_{\text{SL}} = \frac{3Gn(m_2 + \mu/3)}{2c^2 a j^2(e)}. \quad (20)$$

In the presence of a tertiary companion, the orbital axis $\hat{\mathbf{L}}$ of the inner binary precesses around $\hat{\mathbf{L}}_{\text{out}}$ with rate $d\Omega/dt$ and nutates with varying I [see Eqs. (5) and (79)]. To analyze the dynamics of the spin vector, we go to the co-rotating frame with $\hat{\mathbf{L}}$ about $\hat{\mathbf{L}}_{\text{out}}$, in which Eq. (19) becomes

$$\left(\frac{d\mathbf{S}}{dt}\right)_{\text{rot}} = \mathbf{\Omega}_e \times \mathbf{S}, \quad (21)$$

where we have defined an effective rotation vector

$$\mathbf{\Omega}_e \equiv \Omega_L \hat{\mathbf{L}}_{\text{out}} + \Omega_{\text{SL}} \hat{\mathbf{L}}, \quad (22)$$

with [see Eq. (5)]

$$\Omega_L \equiv -\frac{d\Omega}{dt}. \quad (23)$$

In this rotating frame, the plane spanned by $\hat{\mathbf{L}}_{\text{out}}$ and $\hat{\mathbf{L}}$ is constant in time, only the inclination angle I can vary.

3.1 Nondissipative Dynamics

We first consider the limit where dissipation via GW radiation is completely neglected ($t_{\text{GW}}(e) \rightarrow \infty$). Then $\mathbf{\Omega}_e$ is exactly periodic with period P_{LK} [see Eq. (18)]. We can rewrite Eq. (21) in Fourier components

$$\left(\frac{d\mathbf{S}}{dt}\right)_{\text{rot}} = \left[\bar{\mathbf{\Omega}}_e + \sum_{N=1}^{\infty} \mathbf{\Omega}_{eN} \cos(N\Omega_{\text{LK}}t) \right] \times \mathbf{S}. \quad (24)$$

Note that $\bar{\mathbf{\Omega}}_e$ is the zeroth Fourier component, where the bar denotes an average over a LK cycle. We have adopted the convention where $t = 0$ is the time of maximum eccentricity of the LK cycle, so that Eq. (24) does not have $\sin(N\Omega_{\text{LK}}t)$ terms.

This system superficially resembles that considered in [Storch & Lai \(2015\)](#) (SL15), who studied the dynamics of the spin axis of a star when driven by a giant planet undergoing LK oscillations (see also [Storch et al. 2014, 2017](#)). In their system, the spin-orbit coupling arises from Newtonian interaction between the planet (M_p) and the rotation-induced stellar quadrupole ($I_{\text{out}} - I_1$), and the spin precession frequency is

$$\Omega_{\text{SL}}^{(\text{Newtonian})} = -\frac{3GM_p(I_{\text{out}} - I_1) \cos \theta_{\text{sl}}}{2a^3 j^3(e) I_3 \Omega_s}, \quad (25)$$

where $I_3 \Omega_s$ is the spin angular momentum of the star. SL15 showed that under some conditions that depend on a dimensionless adiabaticity parameter (roughly the ratio between the magnitudes of $\Omega_{\text{SL}}^{(\text{Newtonian})}$ and Ω_L when factoring out the eccentricity and obliquity dependence), the stellar spin axis can vary chaotically. One strong indicator of chaos in their study is the presence of irregular, fine structure in a bifurcation diagram [Fig. 1 of [Storch & Lai \(2015\)](#)] that shows the values of the spin-orbit misalignment angle θ_{sl} when varying system parameters in the “transadiabatic” regime, where the adiabaticity parameter crosses unity.

To generate an analogous bifurcation diagram for our problem,

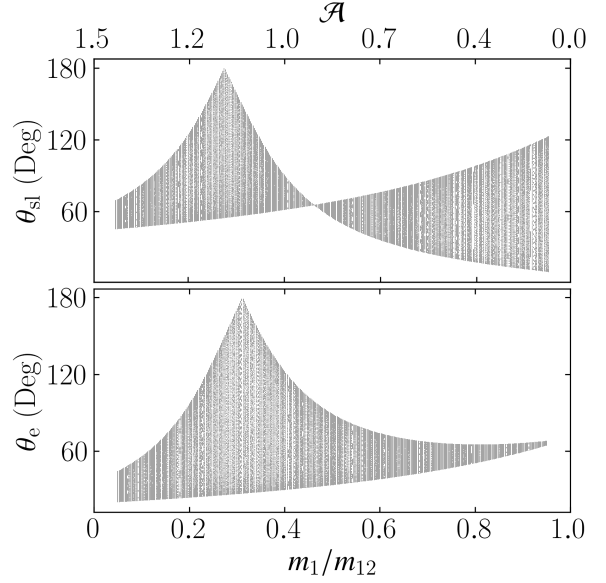


Figure 3. Bifurcation diagram for the BH spin orientation during LK oscillations. The physical parameters are $m_{12} = 60M_{\odot}$, $m_3 = 3 \times 10^7 M_{\odot}$, $a = 0.1$ AU, $e_0 = 10^{-3}$, $I_0 = 70^\circ$, $a_{\text{out}} = 300$ AU, $e_{\text{out}} = 0$, and initial condition $\theta_{\text{sl},0} = 0$. For each mass ratio m_1/m_{12} , the orbit-spin system is solved over 500 LK cycles, and both θ_{sl} (the angle between \mathbf{S} and $\hat{\mathbf{L}}$) and θ_e [defined by Eq. (26)] are sampled at every eccentricity maximum and are plotted. The top axis shows the adiabaticity parameter \mathcal{A} as defined by Eq. (30). Note that for a given m_{12} , changing the mass ratio m_1/m_{12} only changes the spin evolution and not the orbital evolution.

we consider a sample system with $m_{12} = 60M_{\odot}$, $m_3 = 3 \times 10^7 M_{\odot}$, $a = 0.1$ AU, $e_0 = 10^{-3}$, $I_0 = 70^\circ$, $a_{\text{out}} = 300$ AU, $e_{\text{out}} = 0$, and initial $\theta_{\text{sl}} = 0$. We then evolve Eq. (21) together with the orbital evolution equations [Eqs. (3–7) without the GW terms] while sampling both θ_{sl} and θ_e at eccentricity maxima, where θ_e is given by

$$\cos \theta_e = \frac{\bar{\mathbf{\Omega}}_e}{\Omega_e} \cdot \mathbf{S}. \quad (26)$$

We repeat this procedure with different mass ratios m_1/m_{12} of the inner binary, which only changes Ω_{SL} without changing the orbital evolution (note that the LK oscillation depends only on m_{12} and not on individual masses of the inner binary). Analogous to SL15, we consider systems with a range of the adiabaticity parameter \mathcal{A} [to be defined later in Eq. (30)] that crosses order unity. The fiducial system of Fig. 1 does not serve this purpose because the initial Ω_{SL} is too small. Our result is depicted in Fig. 3.

While our bifurcation diagram has interesting structure, the features are all regular. This is in contrast to the star-planet system studied by SL15 (see their Fig. 1). A key difference is that in our system, Ω_{SL} does not depend on θ_{sl} , while for the planet-star system, $\Omega_{\text{SL}}^{(\text{Newtonian})}$ does, and this latter feature introduces nonlinearity to the dynamics.

A more formal understanding of the dynamical behavior of our spin-orbit system comes from Floquet theory ([Floquet 1883](#); [Chicone 2006](#)), as Eq. (21) is a linear system with periodic coefficients (the system studied in SL15 is nonlinear). By Floquet’s theorem, when a linear system with periodic coefficients is inte-

grated over a period, the evolution can be described by the linear transformation

$$\mathbf{S}(t + P_{\text{LK}}) = \tilde{\mathbf{M}}\mathbf{S}(t), \quad (27)$$

where $\tilde{\mathbf{M}}$ is called the *monodromy matrix* and is independent of \mathbf{S} .

For our system, while $\tilde{\mathbf{M}}$ can be easily defined, it cannot be evaluated in closed form. Instead, we can reason directly about the general properties of $\tilde{\mathbf{M}}$: it must be a proper orthogonal matrix, or a rotation matrix, as it represents the effect of many infinitesimal rotations, each about the instantaneous $\boldsymbol{\Omega}_e$ ¹. Therefore, over each period P_{LK} , the dynamics of \mathbf{S} are equivalent to a rotation about a fixed axis, prohibiting chaotic behavior.

Another traditional indicator of chaos is a positive Lyapunov exponent, obtained when the separation between nearby trajectories diverges *exponentially* in time. In Floquet theory, the Lyapunov exponent is the logarithm of the largest eigenvalue of the monodromy matrix. Since $\tilde{\mathbf{M}}$ is a rotation matrix in our problem, the Lyapunov exponent must be 0, indicating no chaos. We have verified this numerically.

3.2 Spin Dynamics With GW Dissipation

When t_{GW} is finite, the coefficients $\boldsymbol{\Omega}_{eN}$, including $\bar{\boldsymbol{\Omega}}_e$ [see Eq. (24)], are no longer constant, but change over time. For “smooth” mergers (satisfying $t_{\text{GW}}(e_{\text{max}}) \gg t_{\text{LK}}/j(e_{\text{max}})$; see Section 2), the binary goes through a sequence of LK cycles, and the coefficients vary on the LK-averaged orbital decay time $t_{\text{GW}}(e_{\text{max}})/j(e_{\text{max}})$. As the LK oscillation freezes, we have $\boldsymbol{\Omega}_e \simeq \bar{\boldsymbol{\Omega}}_e$ (and $\boldsymbol{\Omega}_{eN} \simeq 0$ for $N \geq 1$), which evolves on timescale $t_{\text{GW}}(e)$ as the orbit decays and circularizes.

Once a is sufficiently small that $\Omega_{\text{SL}} \gg \Omega_{\text{L}}$, it can be seen from Eqs. (21–22) that $\theta_e = \theta_{\text{sl}}$ is constant, i.e. the spin-orbit misalignment angle is frozen (see bottom right panel of Fig. 1). This is the “final” spin-orbit misalignment, although the binary may still be far from the final merger. Note that at such separations, $\epsilon_{\text{GR}} \gg 1$ as well since $\Omega_{\text{SL}} \sim \Omega_{\text{GR}}$, and so LK eccentricity excitation is suppressed. For the fiducial examples depicted in Figs. 1–2, we stop the simulation at $a = 0.5$ AU, as θ_{sl} has converged to its final value.

3.3 Spin Dynamics Equation in Component Form

For later analysis, it is useful to write Eq. (24) in component form. To do so, we define inclination angle \bar{I}_e as the angle between $\bar{\boldsymbol{\Omega}}_e$ and \mathbf{L}_{out} as shown in Fig. 4. To express \bar{I}_e algebraically, we define LK-averaged quantities

$$\overline{\Omega_{\text{SL}} \sin I} \equiv \bar{\Omega}_{\text{SL}} \sin \bar{I}, \quad \overline{\Omega_{\text{SL}} \cos I} \equiv \bar{\Omega}_{\text{SL}} \cos \bar{I}. \quad (28)$$

It then follows from Eq. (22) that

$$\tan \bar{I}_e = \frac{\mathcal{A} \sin \bar{I}}{1 + \mathcal{A} \cos \bar{I}}, \quad (29)$$

where \mathcal{A} is the adiabaticity parameter, given by

$$\mathcal{A} \equiv \frac{\bar{\Omega}_{\text{SL}}}{\Omega_{\text{L}}}. \quad (30)$$

¹ More formally, $\tilde{\mathbf{M}} = \tilde{\Phi}(P_{\text{LK}})$ where $\tilde{\Phi}(t)$ is the *principal fundamental matrix solution*: the columns of $\tilde{\Phi}$ are solutions to Eq. (21) and $\tilde{\Phi}(0)$ is the identity. By linearity, the columns of $\tilde{\Phi}(t)$ remain orthonormal, while its determinant does not change, so $\tilde{\mathbf{M}}$ is a proper orthogonal matrix, or a rotation matrix.

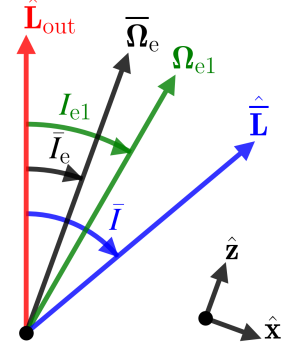


Figure 4. Definition of angles in the problem, shown in plane of the two angular momenta \mathbf{L}_{out} and \mathbf{L} . Here, $\bar{\mathbf{L}}$ is the suitably averaged \mathbf{L} with inclination \bar{I} defined by Eq. (28), $\bar{\boldsymbol{\Omega}}_e$ is the LK-averaged $\boldsymbol{\Omega}_e$, and $\boldsymbol{\Omega}_{e1}$ is the first harmonic component (see Eqs. (22) and (24)). Note that for $I_0 > 90^\circ$ (and $\bar{I} > 90^\circ$), we choose $\bar{I}_e \in (90^\circ, 180^\circ)$ so that $\bar{\Omega}_e > 0$ (since $\Omega_{\text{L}} < 0$). The bottom right shows our choice of coordinate axes with $\hat{\mathbf{z}} \propto \bar{\boldsymbol{\Omega}}_e$.

Note that in Eq. (29), \bar{I}_e is defined in the domain $[0^\circ, 180^\circ]$, i.e. $\bar{I}_e \in (0, 90)$ when $\tan \bar{I}_e > 0$ and $\bar{I}_e \in (90, 180)$ when $\tan \bar{I}_e < 0$.

We now choose a non-inertial coordinate system where $\hat{\mathbf{z}} \propto \bar{\boldsymbol{\Omega}}_e$ and $\hat{\mathbf{x}}$ lies in the plane of \mathbf{L}_{out} and \mathbf{L} (see Fig. 4). In this reference frame, the spin orientation is specified by the polar angle $\bar{\theta}_e$ as defined above in Eq. (35), and the equation of motion becomes

$$\left(\frac{d\mathbf{S}}{dt} \right)_{\text{xyz}} = \left[\bar{\Omega}_e \hat{\mathbf{z}} + \sum_{N=1}^{\infty} \boldsymbol{\Omega}_{eN} \cos(N\Omega_{\text{LK}}t) \right] \times \mathbf{S} - \dot{\bar{I}}_e \hat{\mathbf{y}} \times \mathbf{S}. \quad (31)$$

One further simplification lets us cast this vector equation of motion into a scalar form. Break \mathbf{S} into components $\mathbf{S} = S_x \hat{\mathbf{x}} + S_y \hat{\mathbf{y}} + \cos \bar{\theta}_e \hat{\mathbf{z}}$ and define complex variable

$$S_{\perp} \equiv S_x + iS_y. \quad (32)$$

Then, we can rewrite Eq. (31) as

$$\frac{dS_{\perp}}{dt} = i\bar{\Omega}_e S_{\perp} - \dot{\bar{I}}_e \cos \bar{\theta}_e + \sum_{N=1}^{\infty} \left[\cos(\Delta I_{eN}) S_{\perp} - i \cos \bar{\theta}_e \sin(\Delta I_{eN}) \right] \Omega_{eN} \cos(N\Omega_{\text{LK}}t), \quad (33)$$

where Ω_{eN} is the magnitude of the vector $\boldsymbol{\Omega}_{eN}$ [see Eq. (24)] and $\Delta I_{eN} = I_{eN} - \bar{I}_e$ where I_{eN} is the angle between $\boldsymbol{\Omega}_{eN}$ and \mathbf{L}_{out} (see Fig. 4).

4 ANALYSIS: APPROXIMATE ADIABATIC INVARIANT

In general, Eqs. (24) and (33) are difficult to study analytically. In this section, we neglect the harmonic terms and focus on how the varying $\bar{\boldsymbol{\Omega}}_e$ affects the evolution of the BH spin axis. The effect of the harmonic terms is studied in Section 5.

4.1 The Adiabatic Invariant

When neglecting the $N \geq 1$ harmonic terms, Eq. (24) reduces to

$$\left(\frac{d\bar{\mathbf{S}}}{dt} \right)_{\text{rot}} = \bar{\boldsymbol{\Omega}}_e \times \bar{\mathbf{S}}. \quad (34)$$

It is not obvious to what extent the analysis of Eq. (34) is applicable to Eq. (24). From our numerical calculations, we find that

the LK-average of \mathbf{S} often evolves following Eq. (34), motivating our notation $\bar{\mathbf{S}}$. Over timescales shorter than the LK period P_{LK} , Eq. (34) loses accuracy as the evolution of \mathbf{S} itself is dominated by the $N \geq 1$ harmonics we have neglected. An intuitive interpretation of this result is that the $N \geq 1$ harmonics vanish when integrating Eq. (24) over a LK cycle.

Eq. (34) has one desirable property: $\bar{\theta}_e$, given by

$$\cos \bar{\theta}_e \equiv \frac{\bar{\Omega}_e}{\Omega_e} \cdot \bar{\mathbf{S}}, \quad (35)$$

is an adiabatic invariant. The adiabaticity condition requires the precession axis evolve slowly compared to the precession frequency at all times, i.e.

$$\left| \frac{d\bar{\mathbf{I}}_e}{dt} \right| \ll \bar{\Omega}_e. \quad (36)$$

For our fiducial example depicted in Fig. 1, the values of $\dot{\bar{\mathbf{I}}}_e$ and $\bar{\Omega}_e$ are shown in the top panel of Fig. 5, and the evolution of $\bar{\theta}_e$ in the bottom panel. The net change in $\bar{\theta}_e$ in this simulation is 0.01° , small as expected since $|\dot{\bar{\mathbf{I}}}_e| \ll \bar{\Omega}_e$ at all times.

4.2 Deviation from Adiabaticity

The extent to which $\bar{\theta}_e$ is conserved depends on how well Eq. (36) is satisfied. In this subsection, we derive a bound on the total non-conservation of $\bar{\theta}_e$, then in the next subsection we show how this bound can be estimated from initial conditions.

When neglecting harmonic terms, the scalar equation of motion Eq. (33) becomes

$$\frac{dS_\perp}{dt} = i\bar{\Omega}_e S_\perp - \dot{\bar{\mathbf{I}}}_e \cos \bar{\theta}_e. \quad (37)$$

This can be solved in closed form. Defining

$$\Phi(t) \equiv \int_{t_0}^t \bar{\Omega}_e dt, \quad (38)$$

we obtain the solution between the initial time t_0 and the final time t_f :

$$e^{-i\Phi} S_\perp \Big|_{t_0}^{t_f} = - \int_{t_0}^{t_f} e^{-i\Phi(\tau)} \dot{\bar{\mathbf{I}}}_e \cos \bar{\theta}_e d\tau. \quad (39)$$

Recalling $|S_\perp| = \sin \bar{\theta}_e$ and analyzing Eq. (39), we see that $\bar{\theta}_e$ oscillates about its initial value with semi-amplitude

$$|\Delta \bar{\theta}_e| \sim \left| \frac{\dot{\bar{\mathbf{I}}}_e}{\bar{\Omega}_e} \right|. \quad (40)$$

In the adiabatic limit [Eq. (36)], $\bar{\theta}_e$ is indeed conserved, as the right-hand side of Eq. (40) goes to zero. The bottom panel of Fig. 5 shows $\Delta \bar{\theta}_e$ for the fiducial example. Note that $\bar{\theta}_e$ is indeed mostly constant where Eq. (40) predicts small oscillations.

If we denote $|\Delta \bar{\theta}_e|_f$ to be the net change in $\bar{\theta}_e$ over $t \in [t_0, t_f]$, we can give a loose bound

$$|\Delta \bar{\theta}_e|_f \lesssim \left| \frac{\dot{\bar{\mathbf{I}}}_e}{\bar{\Omega}_e} \right|_{\text{max}}. \quad (41)$$

Inspection of Fig. 5 indicates that the spin dynamics are mostly uninteresting except near the peak of $|\dot{\bar{\mathbf{I}}}_e|$, which occurs where $\bar{\Omega}_{\text{SL}} \approx |\Omega_{\text{L}}|$. We present a zoomed-in view of dynamical quantities near

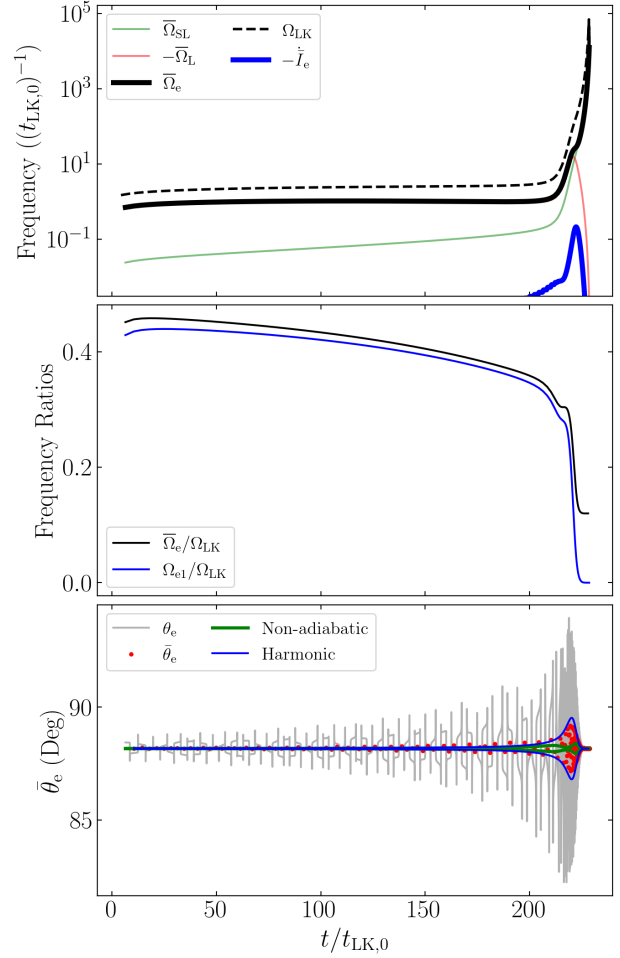


Figure 5. The same simulation as depicted in Fig. 1 but showing the calculated quantities relevant to the theory of the spin evolution. Top: the four characteristic frequencies of the system and $d\bar{\mathbf{I}}_e/dt$. Middle: the frequency ratios between the zeroth and first Fourier components of Ω_e to the LK frequency Ω_{LK} . Bottom: Time evolution of θ_e [grey line; Eq. (26)], $\bar{\theta}_e$ [red dots; Eq. (35)], as well as estimates of the deviations from perfect conservation of $\bar{\theta}_e$ due to nonadiabaticity [green, Eq. (40)] and due to resonances with the $N = 1$ harmonic [blue, Eq. (74)].

the peak of $\dot{\bar{\mathbf{I}}}_e$ in Fig. 6. In particular, in the bottom-rightmost panel, we see that the fluctuations in $\bar{\theta}_e$ are dominated by a second contribution, the subject of the discussion in Section 5.

For comparison, we show in Fig. 7 a more rapid binary merger starting with $I_0 = 90.2^\circ$, for which $|\Delta \theta_e|_f \approx 2^\circ$. If we again examine the bottom-rightmost panel, we see that the net $|\Delta \bar{\theta}_e|_f$ obeys Eq. (41).

4.3 Estimate of Deviation from Adiabaticity from Initial Conditions

To estimate Eq. (41) as a function of initial conditions, we first differentiate Eq. (29),

$$\dot{\bar{\mathbf{I}}}_e = \left(\frac{\mathcal{A}}{\bar{\mathcal{A}}} \right) \frac{\mathcal{A} \sin \bar{I}}{1 + 2\mathcal{A} \cos \bar{I} + \mathcal{A}^2}. \quad (42)$$

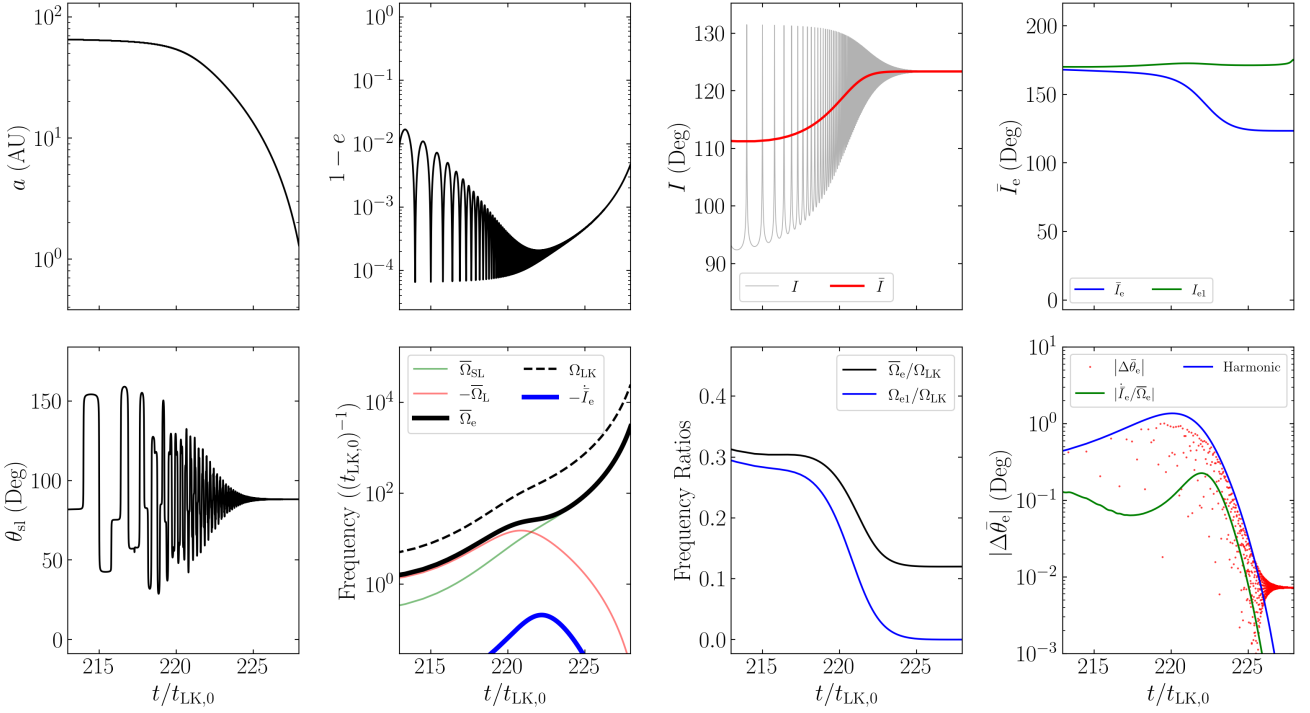


Figure 6. The same simulation as Fig. 1 but zoomed in on the region around $\mathcal{A} \equiv \bar{\Omega}_{\text{SL}}/\bar{\Omega}_{\text{L}} \approx 1$ and showing a wide range of relevant quantities. The first three panels in the upper row depict a , e , I and \bar{I} as in Fig. 1, while the fourth shows \bar{I}_e [Eq. (29)] and I_{e1} . The bottom four panels depict θ_{sl} , the four characteristic frequencies of the system and $d\bar{I}_e/dt$ [Eqs. 22 and (23)] (as in the top panel of Fig. 5), the relevant frequency ratios (as in the middle panel of Fig. 5), and the deviation of θ_e from its initial value compared to the predictions of Eqs. (40) and (74).

It also follows from Eq. (22) that

$$\bar{\Omega}_e = \left| \bar{\Omega}_{\text{L}} \right| \left(1 + 2\mathcal{A} \cos \bar{I} + \mathcal{A}^2 \right)^{1/2}, \quad (43)$$

from which we obtain

$$\left| \frac{\dot{\bar{I}}_e}{\bar{\Omega}_e} \right| = \left(\frac{\mathcal{A}}{\bar{\Omega}_{\text{L}}} \right) \frac{1}{\left| \bar{\Omega}_{\text{L}} \right|} \frac{\mathcal{A} \sin \bar{I}}{\left(1 + 2\mathcal{A} \cos \bar{I} + \mathcal{A}^2 \right)^{3/2}}. \quad (44)$$

Moreover, if we assume the eccentricity is frozen around $e \approx 1$ and use $\cos^2 \omega \approx 1/2$ in $|\dot{\Omega}_{\text{L}}| = |d\dot{\Omega}/dt|$, we obtain the estimate

$$\begin{aligned} \mathcal{A} &\approx \frac{3Gn(m_2 + \mu/3)}{2c^2 a j^2(e)} \left[\frac{15 \cos \bar{I}}{8t_{\text{LK}} j(e)} \right]^{-1} \\ &\approx \frac{4}{5} \frac{G(m_2 + \mu/3)m_{12}\tilde{a}_{\text{out}}^3}{c^2 m_3 a^4 j(e) \cos \bar{I}}, \end{aligned} \quad (45)$$

$$\frac{\dot{\mathcal{A}}}{\mathcal{A}} = -4 \left(\frac{\dot{a}}{a} \right)_{\text{GW}} + \frac{e}{j^2(e)} \left(\frac{de}{dt} \right)_{\text{GW}}. \quad (46)$$

With these, we see that Eq. (44) is largest around $\mathcal{A} \approx 1$, and so we find that the maximum $\left| \dot{\bar{I}}_e / \bar{\Omega}_e \right|$ is given by

$$\left| \frac{\dot{\bar{I}}_e}{\bar{\Omega}_e} \right|_{\text{max}} \approx \left| \frac{\dot{\mathcal{A}}}{\mathcal{A}} \right| \frac{1}{\left| \bar{\Omega}_{\text{L}} \right|} \frac{\sin \bar{I}}{(2 + 2 \cos \bar{I})^{3/2}}. \quad (47)$$

To evaluate this, we make two assumptions: (i) \bar{I} is approximately constant (see the third panels of Figs. 6 and 7), and (ii) $j(e)$ evaluated at $\mathcal{A} \approx 1$ can be approximated as a constant multiple of

the initial $j(e_{\text{max}})$, i.e.

$$j_{\star} \equiv j(e_{\star}) = f \sqrt{\frac{5}{3}} \cos^2 I_0, \quad (48)$$

where the star subscript denotes evaluation at $\mathcal{A} \approx 1$ and $f > 1$ is a constant. Eq. (48) assumes that I_0 far enough from 90° that the GR effect is unimportant in determining e_{max} . The value of f turns out to be relatively insensitive to I_0 .

Using Eq. (46) and approximating $e_{\star} \approx 1$ in Eqs. (11) and (12) give

$$\left[\frac{\dot{\mathcal{A}}}{\mathcal{A}} \right]_{\star} \approx \frac{G^3 \mu m_{12}^2}{c^5 a_{\star}^4 j_{\star}^7} \frac{595}{3}. \quad (49)$$

To determine a_{\star} , we require Eq. (45) to give $\mathcal{A} = 1$ for a_{\star} and j_{\star} . Taking this and Eq. (49), we rewrite Eq. (44) as

$$\left| \frac{\dot{\bar{I}}_e}{\bar{\Omega}_e} \right|_{\text{max}} \approx \frac{595 \sin \bar{I} |\cos \bar{I}|^{3/8}}{36 (\cos \bar{I} + 1)^{3/2}} \left[\frac{8000 G^9 m_{12}^9 m_3^3 \mu^8}{\tilde{a}_{\text{out}}^9 j_{\star}^{37} c^{18} (m_2 + \mu/3)^{11}} \right]^{1/8}. \quad (50)$$

We can also calculate $\left| \dot{\bar{I}}_e / \bar{\Omega}_e \right|$ from numerical simulations. Taking characteristic $\bar{I} \approx 120^\circ$ (Figs. 6 and 7 show that this holds across a range of I_0), we fit the last remaining free parameter f [Eq. (48)] to the data from numerical simulations. This yields $f \approx 2.72$, leading

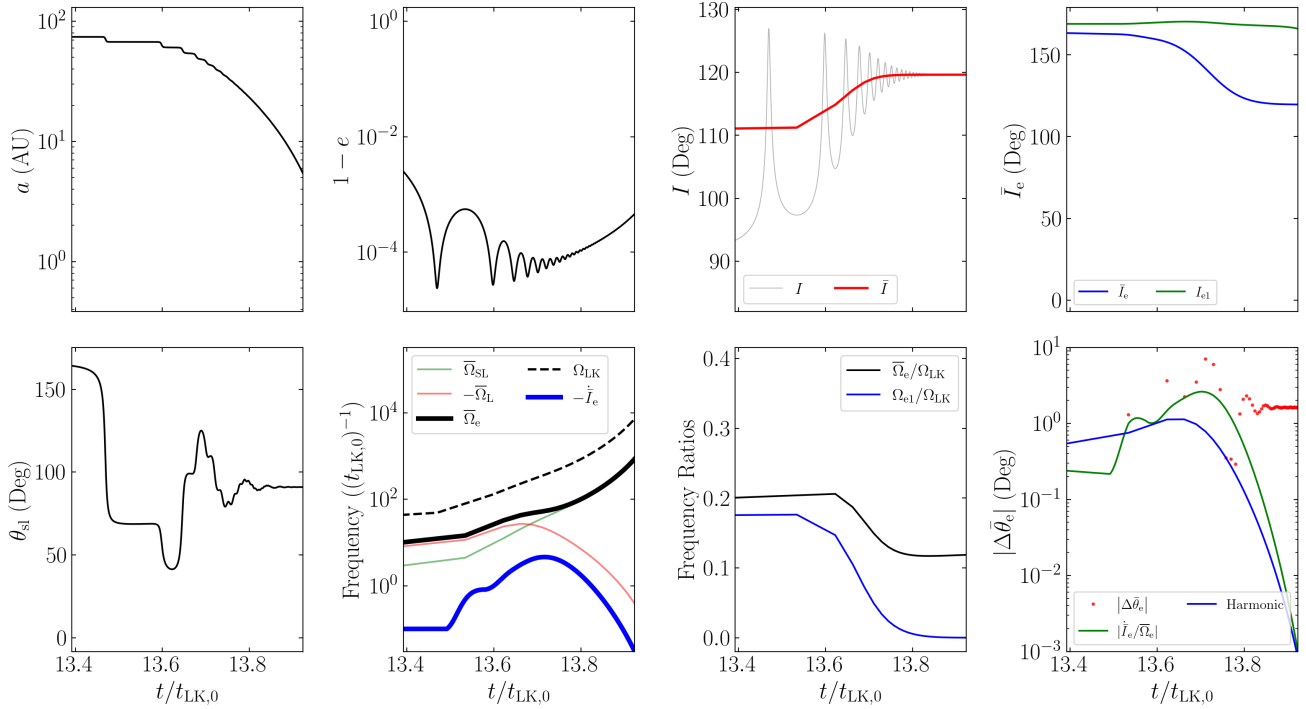


Figure 7. Same as Fig. 6 except for $I_0 = 90.2^\circ$ (and all other parameters are the same as in Fig. 1), corresponding to a faster coalescence. The total change in $\bar{\theta}_e$ for this simulation is $\approx 2^\circ$.

to

$$\left| \frac{\dot{\bar{I}}_e}{\bar{\Omega}_e} \right|_{\max} \approx 0.98^\circ \left(\frac{\cos I_0}{\cos(90.3^\circ)} \right)^{-37/8} \left(\frac{\tilde{a}_{\text{out}}}{2.2 \text{ pc}} \right)^{-9/8} \times \left(\frac{m_3}{3 \times 10^7 M_\odot} \right)^{3/8} \left(\frac{m_{12}^9 \mu^8 / (m_2 + \mu/3)^{11}}{(28.64 M_\odot)^6} \right)^{1/8}. \quad (51)$$

Fig. 8 shows that when the merger time T_m is much larger than the initial LK timescale, Eq. (51) provides an accurate estimate for $|\dot{\bar{I}}_e/\bar{\Omega}_e|_{\max}$ when compared with numerical results.

In the above, we have assumed that the system evolves through $\mathcal{A} \approx 1$ when the eccentricity is mostly frozen (see Fig. 1 for an indication of how accurate this is for the parameter space explored in Fig. 8). It is also possible that $\mathcal{A} \approx 1$ occurs when the eccentricity is still undergoing substantial oscillations. In fact, Eq. (51) remains accurate in this case when replacing e with e_{\max} , due to the following analysis. Recall that when $e_{\min} \ll e_{\max}$, the binary spends a fraction $\sim j(e_{\max})$ of the LK cycle near $e \approx e_{\max}$. This fraction of the LK cycle dominates both GW dissipation and $\bar{\Omega}_e$ precession. Thus, both $\dot{\bar{I}}_e$ and $\bar{\Omega}_e$ in the oscillating- e regime can be evaluated by setting $e \approx e_{\max}$ and multiplying by a prefactor of $j(e_{\max})$. This factor cancels when computing the quotient $|\dot{\bar{I}}_e/\bar{\Omega}_e|$.

The accuracy of Eq. (51) in bounding $|\Delta \bar{\theta}_e|_f$ is shown in Fig. 9, where we carry out simulations for a range of I_0 , and for each I_0 we consider 100 different, isotropically distributed initial orientations for \mathbf{S} (thus sampling a wide range of initial $\bar{\theta}_e$). Note that conservation of $\bar{\theta}_e$ is generally much better than Eq. (51) predicts. This is because cancellation of phases in Eq. (39) is generally more efficient than Eq. (51) assumes (recall that Eq. (40) only provides an estimate for the amplitude of “local” oscillations of $\bar{\theta}_e$). Never-

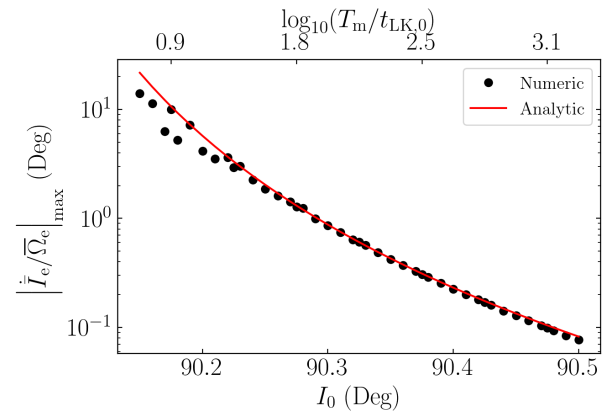


Figure 8. Comparison of $|\dot{\bar{I}}_e/\bar{\Omega}_e|_{\max}$ obtained from simulations and from the analytical expression Eq. (51), where we take $f = 2.72$ in Eq. (48). The coalescence time T_m is shown along the top axis of the plot in units of the characteristic LK timescale at the start of inspiral $t_{\text{LK},0}$. The agreement between the analytical and numerical results is excellent for $T_m \gg t_{\text{LK},0}$.

theless, it is clear that Eq. (51) provides a robust upper bound of $|\Delta \bar{\theta}_e|_f$, and serves as a good indicator for the breakdown of adiabatic invariance.

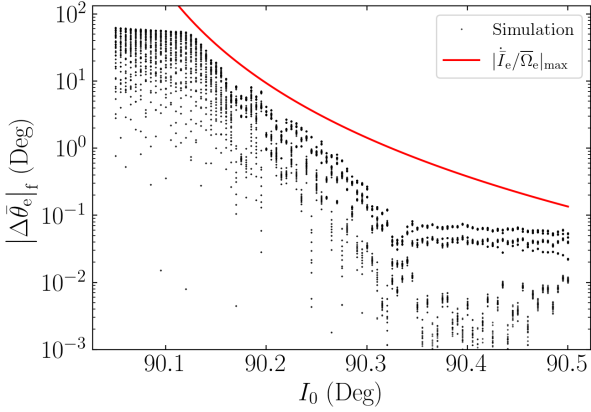


Figure 9. Net change in $\bar{\theta}_e$ over the binary inspiral as a function of initial inclination I_0 . For each I_0 , 100 simulations are run for \mathbf{S} on a uniform, isotropic grid. Plotted for comparison is the bound $|\Delta\bar{\theta}_e|_f \lesssim |\bar{\dot{I}}_e/\bar{\Omega}_e|_{\max}$, using the analytical expression given by Eq. (51). It is clear that the expression provides a robust upper bound for the non-conservation of $\bar{\theta}_e$ due to nonadiabatic effects. Note that at the right of the plot, the numerical $|\Delta\bar{\theta}_e|_f$ saturates; this is because we compute the initial $\bar{\Omega}_e$ (in order to evaluate the initial $\bar{\theta}_e$) without GW dissipation, and such a procedure inevitably introduces fuzziness in $\bar{\theta}_e$.

4.4 Origin of the $\theta_{\text{sl},f} = 90^\circ$ Attractor

Using the approximate adiabatic invariant, we can now understand the origin of the $\theta_{\text{sl},f} = 90^\circ$ attractor as shown in Fig. 2.

Recall from Eq. (22)

$$\begin{aligned}\bar{\Omega}_e &= \bar{\Omega}_L \hat{\mathbf{L}}_{\text{out}} + \bar{\Omega}_{\text{SL}} \hat{\mathbf{L}}, \\ &= (\bar{\Omega}_L + \bar{\Omega}_{\text{SL}} \cos \bar{I}) \hat{\mathbf{Z}} + \bar{\Omega}_{\text{SL}} \sin \bar{I} \hat{\mathbf{X}},\end{aligned}\quad (52)$$

where $\hat{\mathbf{Z}} = \hat{\mathbf{L}}_{\text{out}}$ and $\hat{\mathbf{X}}$ is perpendicular to $\hat{\mathbf{Z}}$ in the $\hat{\mathbf{L}}_{\text{out}}-\hat{\mathbf{L}}$ plane. Note that

$$\bar{\Omega}_L \propto \frac{\cos \bar{I}}{t_{\text{LK}}} \propto a^{3/2} \cos \bar{I}, \quad (53)$$

$$\bar{\Omega}_{\text{SL}} \propto \frac{1}{a^{5/2}}. \quad (54)$$

Adiabatic invariance implies that $\bar{\theta}_e$, the angle between \mathbf{S} and $\bar{\Omega}_e$ is conserved between $t = t_0$ and $t = t_f$, i.e.

$$\bar{\theta}_{e,f} \simeq \bar{\theta}_{e,0}. \quad (55)$$

At $t = t_f$, $\bar{\Omega}_{\text{SL}} \gg |\bar{\Omega}_L|$ and the spin-orbit misalignment angle θ_{sl} is “frozen”, implying $\bar{\Omega}_e$ is parallel to \mathbf{L} , and so $\bar{\theta}_{e,f} = \theta_{\text{sl},f}$. Eq. (55) then gives

$$\theta_{\text{sl},f} \simeq \bar{\theta}_{e,0}, \quad (56)$$

i.e. the final θ_{sl} is determined by the initial angle between \mathbf{S} and $\bar{\Omega}_e$.

Now, first consider the case where the initial spin \mathbf{S}_0 is aligned with the initial \mathbf{L}_0 . This initial spin is inclined with respect to $\bar{\Omega}_e$ by $\bar{\theta}_{e,0} = |I_0 - \bar{I}_{e,0}|$, where I_0 is the initial inclination angle between \mathbf{L} and \mathbf{L}_{out} and $\bar{I}_{e,0}$ is the initial value of \bar{I}_e . Thus, adiabatic invariance implies

$$\theta_{\text{sl},f} \simeq |I_0 - \bar{I}_{e,0}|. \quad (57)$$

In the special case where the binary initially satisfies $\bar{\Omega}_{\text{SL}} \ll |\bar{\Omega}_L|$

or $|\mathcal{A}_0| \ll 1$, we find that $\bar{\Omega}_e$ is nearly parallel to \mathbf{L}_{out} (for $I_0 < 90^\circ$) or antiparallel to \mathbf{L}_{out} (for $I_0 > 90^\circ$). Thus,

$$\theta_{\text{sl},f} = \begin{cases} I_0 & I_0 < 90^\circ, \\ 180^\circ - I_0 & I_0 > 90^\circ. \end{cases} \quad (58)$$

Since LK-induced mergers necessarily require I_0 close to 90° , we find that $\theta_{\text{sl},f}$ is “attracted” to 90° .

Eq. (56) can be applied to more general initial spin orientations. For initial $|\mathcal{A}_0| \ll 1$ (as required for LK-induced mergers), $\bar{\Omega}_{e,0}$ is parallel to $\pm \mathbf{L}_{\text{out}}$. Suppose the initial inclination between \mathbf{S} and \mathbf{L}_{out} is $\theta_{\text{s,out},0}$, then $\bar{\theta}_{e,0} = \theta_{\text{s,out},0}$ or $180^\circ - \theta_{\text{s,out},0}$ (depending on whether $I_0 < 90^\circ$ or $I_0 > 90^\circ$). Thus,

$$\theta_{\text{sl},f} \simeq \begin{cases} \theta_{\text{s,out},0} & I_0 < 90^\circ, \\ 180^\circ - \theta_{\text{s,out},0} & I_0 > 90^\circ, \end{cases} \quad (59)$$

(see also Yu et al. 2020).

So far, we have analyzed the $\theta_{\text{sl},f}$ distribution for smooth mergers. Next, we can consider rapid mergers, for which $\bar{\theta}_e$ conservation is imperfect. We expect

$$|\theta_{\text{sl},f} - \bar{\theta}_{e,0}| \lesssim |\Delta\bar{\theta}_e|_f. \quad (60)$$

where $|\Delta\bar{\theta}_e|_f$ is given by Eq. (51). This is shown as the black dotted line in Fig. 2, and we see it predicts the maximum deviation of $\theta_{\text{sl},f}$ from $\sim 90^\circ$ except very near $I_0 = 90^\circ$. This is expected, as Eq. (51) is not very accurate very near $I_0 = 90^\circ$, where it diverges (see Fig. 9).

When $I_0 = 90^\circ$ exactly, Fig. 2 shows that $\theta_{\text{sl},f} = 0^\circ$. This can be understood: $I_0 = 90^\circ$ gives $dI/dt = 0$ by Eq. (79), so $I = 90^\circ$ for all time. This then implies $d\Omega/dt = 0$ [Eq. (5)], implying that \mathbf{L} is constant. Thus, \mathbf{L} is fixed as \mathbf{S} precesses around it, and θ_{sl} can never change. In Fig. 2, we take $\theta_{\text{sl},0} = 0$, so $\theta_{\text{sl},f} = 0$.

Finally, Fig. 2 shows that the actual $\theta_{\text{sl},f}$ are oscillatory within the envelope bounded by Eq. (60) above. This can also be understood: Eq. (41) only bounds the maximum of the absolute value of the change in $\bar{\theta}_e$, while the actual change depends on the initial and final complex phases of S_\perp in Eq. (39), denoted $\Phi(t_0)$ and $\Phi(t_f)$. When $\theta_{\text{sl},0} = 0$, we have $\Phi(t_0) = 0$, as \mathbf{S} starts in the $\hat{\mathbf{x}}-\hat{\mathbf{z}}$ plane. Then, as I_0 is smoothly varied, the final phase $\Phi(t_f)$ must also vary smoothly [since $\bar{\Omega}_e$ in Eq. (38) is a continuous function, $\Phi(t)$ must be as well], so the total phase difference between the initial and final values of S_\perp varies smoothly. This means the total change in $\bar{\theta}_e$ will fluctuate smoothly between $\pm |\Delta\bar{\theta}_e|_f$ as I_0 is changed, giving rise to the sinusoidal shape seen in Fig. 2.

5 ANALYSIS: EFFECT OF RESONANCES

In the previous section, we showed that the $\theta_{\text{sl},f}$ distribution can be well understood when assuming the $N \geq 1$ Fourier harmonics in Eq. (24) can be neglected. In this section, we study the effects of these neglected terms and their effect in the LK-induced and LK-enhanced regimes.

For simplicity, we ignore the effects of GW dissipation in this section and assume the system is exactly periodic (so $\dot{I}_e = 0$). The scalar equation of motion Eq. (33) is then:

$$\begin{aligned}\frac{dS_\perp}{dt} &= i\bar{\Omega}_e S_\perp + \sum_{N=1}^{\infty} \left[\cos(\Delta I_{eN}) S_\perp \right. \\ &\quad \left. - i \cos \bar{\theta}_e \sin(\Delta I_{eN}) \right] \Omega_{eN} \cos(N\Omega_{\text{LK}} t).\end{aligned}\quad (61)$$

5.1 Near-Resonance Oscillation Amplitude

We first restrict our analysis to a single Fourier harmonic at a time, indexed by N . Eq. (61) further simplifies to

$$\frac{dS_{\perp}}{dt} = i\bar{\Omega}_e S_{\perp} + \left[\cos(\Delta I_{eN}) S_{\perp} - i \cos \bar{\theta}_e \sin(\Delta I_{eN}) \right] \Omega_{eN} \cos(N\Omega_{LK}t). \quad (62)$$

The general solution to this is given by

$$\begin{aligned} \left[e^{-i\Phi} S_{\perp} \right]_{t_0}^t &= -i \cos \bar{\theta}_e \sin \Delta I_{eN} \int_{t_0}^t \Omega_{eN} \cos(N\Omega\tau) e^{-i\Phi(\tau)} d\tau, \\ &= iA \left[e^{-i\Phi} \right]_{t_0}^t + i\bar{\Omega}_e \int_{t_0}^t e^{-i\Phi(\tau)} d\tau. \end{aligned} \quad (63)$$

where $A = \tan \Delta I_{eN} \cos \bar{\theta}_e$, and

$$\begin{aligned} i\Phi(t) &\equiv \int_{t_0}^t i\bar{\Omega}_e + \cos(N\Omega_{LK}t) \cos(\Delta I_{eN}) \Omega_{eN} dt, \\ &\equiv i\bar{\Omega}_e t + \eta \sin(N\Omega_{LK}t), \end{aligned} \quad (64)$$

where $\eta \equiv (\cos \Delta I_{eN} \Omega_{eN}) / (N\Omega_{LK})$. Eq. (63) shows that $|S_{\perp}|$ is bounded unless the integral $\mathcal{I}(x)$, given by

$$\mathcal{I}(x) = \int_0^x e^{-i\xi - \eta \sin(\beta\xi)} d\xi, \quad (65)$$

grows without bound as $x \rightarrow \infty$, where we have rescaled $x = \bar{\Omega}_e(t - t_0)$ and $\beta = N\Omega_{LK}/\bar{\Omega}_e$.

To see where $\mathcal{I}(x)$ grows without bound, we rewrite

$$\mathcal{I}(x) = \sum_{k=0}^{\infty} \int_0^x (\cos \xi + i \sin \xi) \frac{(-\eta \sin(\beta\xi))^k}{k!} d\xi. \quad (66)$$

These $\sin^k(\beta\xi)$ terms can be expanded using the general trigonometric power-reduction identities (Zwillinger 2002):

$$\sin^{2n} y = \frac{1}{2^{2n}} \binom{2n}{n} + \frac{(-1)^n}{2^{2n-1}} \sum_{k=0}^{n-1} (-1)^k \binom{2n}{k} \cos[2(n-k)y], \quad (67)$$

$$\sin^{2n+1} y = \frac{(-1)^n}{4^n} \sum_{k=0}^n (-1)^k \binom{2n+1}{k} \sin[(2n+1-2k)y]. \quad (68)$$

Due to the orthogonality relations among the trigonometric functions, $\mathcal{I}(x)$ only grows without bound if $\sin^k(\beta\xi)$ contains a $\cos \xi$ or $\sin \xi$ term. Upon inspection, $\sin^k(\beta\xi)$ only contains a term with unit frequency if $\beta = 1/q$ for some integer q and $k \geq q$. When this is the case, we can evaluate $\mathcal{I}(x)$ over one period $x = 2\pi q$ and obtain

$$|\mathcal{I}(2\pi q)| = 2\pi q \left(\frac{\eta^q}{2^q q!} + O\left(\frac{1}{(q+1)!}\right) \right). \quad (69)$$

The higher order corrections arise from the $k \geq q+1$ terms in Eq. (66). Since every period has a fixed, nonzero contribution to $\mathcal{I}(x)$, $|\mathcal{I}(x)|$ grows without bound when

$$\bar{\Omega}_e = Nq\Omega_{LK}. \quad (70)$$

Instead, if β is near but not on a resonance, i.e. $0 < |1 - q\beta| \ll$

1, we can show that the amplitude of oscillation of $|\mathcal{I}(x)|$ is bounded but can become large. If q is even, then the dominant behavior is

$$\begin{aligned} |\mathcal{I}(x)| &\approx \int_0^x \cos \xi \frac{|\eta|^q}{q!} \frac{1}{2^{q-1}} \cos(q\beta\xi) d\xi, \\ &\approx \frac{|\eta|^q}{q!} \frac{1}{2^{q-1}} \int_0^x \frac{1}{2} \left[\cos(\xi(1+q\beta)) + \cos(\xi(1-q\beta)) \right] d\xi, \\ &\lesssim \frac{|\eta|^q}{2^q q!} \frac{1}{|1-q\beta|}. \end{aligned} \quad (71)$$

If q is odd, we use Eq. (68) instead of Eq. (67) and integrate against $i \sin x$ instead of $\cos x$, which results in the same bound on the oscillation amplitude. Thus, we see that if $0 < |1 - q\beta| \ll 1$, i.e. the system is near but not on resonance, S_{\perp} oscillates over a large but finite range.

5.2 Effect of Multiple Resonances

In the previous section, we considered only the effect of a single N . However, if $\bar{\Omega}_e/\Omega_{LK} \approx M$ where M is an integer greater than 1, there are multiple combinations of N and q that satisfy $M = Nq$. We can attempt to understand whether particular combinations of N and q dominate the response in S_{\perp} . We make a few simplifying assumptions: (i) all N harmonics are approximately equal², (ii) $\Omega_{eN} \sim \bar{\Omega}_e$ and $\cos \Delta I_{eN} \approx 1$ (e.g. Figs. 5 and 6), and (iii) the oscillation amplitude of S_{\perp} due to multiple resonances is the sum of the amplitude due to each individual resonance. Under the first two assumptions, Eq. (71) scales like:

$$\max |\mathcal{I}(x)| \propto \frac{\cos^q(\Delta I_{eN}) q^q}{2^q q!}. \quad (72)$$

For $q = 1$ and $q = 2$, this expression changes by a factor of $\cos \Delta I_{eN} \approx 1$. For general q , Stirling's approximation suggests that $\max |\mathcal{I}(x)| \approx (\cos(\Delta I_{eN}) e/2)^q \sim 1$. As such, we conclude that all combinations of N and q satisfying $Nq = M$ result in comparable oscillation amplitudes. Denote the number of such pairs of N and q by $d(M)$, which is just the number of positive divisors of M . Then, by our third assumption above, the total oscillation amplitude is just the sum of these contributions, which we evaluate at $q = 1, N = M$ for simplicity:

$$\left| \left[e^{-i\Phi} S_{\perp} \right]_{t_0}^t \right| \lesssim \frac{d(M)}{2} \left| \frac{A\eta}{\bar{\Omega}_e - M\Omega_{LK}} \right|. \quad (73)$$

Finally, we conclude that the effect of all the Fourier harmonics together causes $\bar{\theta}_e = \sqrt{1 - |S_{\perp}|^2}$ to oscillate with semi-amplitude

$$|\Delta \bar{\theta}_e| \sim \frac{d(N)}{2} \left| \frac{\sin \Delta I_{eN} \Omega_{eN}}{\bar{\Omega}_e - N\Omega_{LK}} \right|, \quad (74)$$

where we have set $M = N$ as $q = 1$. Note that $d(1) = 1$ while $d(2) = 2$. While we have made some crude approximations in deriving Eq. 74, Appendix A3 demonstrates that it is in good agreement with detailed numerical simulations when $N = 1$ or $N = 2$, the two relevant cases for the main text.

² This approximation is suitable for the problem studied in the main text because the only characteristic frequency scale is $j_{\min}^{-1} \gg 1$, so all Fourier harmonics Ω_{eN} for $N \lesssim j_{\min}^{-1}$ are similar.

5.3 Effect of Resonances in LK-Induced Mergers

We first consider the effect of these resonances on the LK-induced regime, using the fiducial parameters. Numerically, we find that $\bar{\Omega}_e < \Omega_{LK}$ for the region of parameter space relevant to LK-induced mergers (see Fig. 10), so we focus on the effect of the $N = 1$ resonance. If, for the entire inspiral, $\bar{\Omega}_e < \Omega_{LK}$ by a sufficient margin that Eq. (74) remains small, then the conservation of $\bar{\theta}_e$ cannot be significantly affected by this resonance. For the fiducial simulation, Fig. 5 shows the ratio $\bar{\Omega}_e/\Omega_{LK}$ in the middle panel (black) and the amplitude of oscillation of $\bar{\theta}_e$ due to the $N = 1$ resonance [Eq. (74)] in the bottom panel (blue). We see that the system is never close to the resonant condition $\bar{\Omega}_e/\Omega_{LK} = 1$, and as a result the total effect of the resonance never exceeds a few degrees.

For a more precise comparison, the bottom-rightmost panel of Fig. 6 compares $|\Delta\bar{\theta}_e|$ in the fiducial simulation to the expected contributions from nonadiabatic [Eq. (40)] and resonant [Eq. (74) for $N = 1$] effects in the regime where $\mathcal{A} \simeq 1$. We see that Eq. (74) for $N = 1$ describes the oscillations in $\bar{\theta}_e$ very well. The agreement is poorer in the bottom-rightmost panel of Fig. 7, as the nonadiabatic effect is much stronger.

It is surprising that the contribution of the resonant terms to the instantaneous $\Delta\bar{\theta}_e$ in the $\mathcal{A} \simeq 1$ regime is dominant over that of the nonadiabatic contribution. In the previous section, we showed that neglecting resonant terms still allows for an accurate prediction of the final $\bar{\theta}_e$ deviation [Eq. (51)]. This implies that the nonadiabatic effect is instead more important than the resonant terms in determining the final deviation. This also requires that a $|\Delta\bar{\theta}_e|$ of up to a few degrees due to the $N \geq 1$ Fourier harmonics not affect the final nonconservation of $\bar{\theta}_e$ by more than $\sim 0.01^\circ$. This differs from the nonadiabatic case, where we find $|\Delta\bar{\theta}_e|_f \sim \max |\Delta\bar{\theta}_e|$. We do not have an explanation for this discrepancy.

5.4 Effect of Resonances in LK-Enhanced Mergers

We turn now to the case of LK-enhanced mergers, as was studied in LL17, where the inner binary is sufficiently compact (~ 0.1 AU) that it can merge in isolation via GW radiation. We consider a set of parameters that has the same $t_{LK,0}$ as the system studied in LL17 but has a tertiary SMBH: $m_1 = m_2 = 30M_\odot$, $a_0 = 0.1$ AU, $e_0 = 10^{-3}$, $m_3 = 3 \times 10^7 M_\odot$, $\tilde{a}_{out} = 300$ AU, and $e_{out} = 0$. We show that the resonances studied above play an important role in shaping the $\theta_{sl,f}$ distribution in this regime.

First, we illustrate the $\theta_{sl,f}$ distribution obtained via numerical simulation, shown as the blue dots in Fig. 11. The prediction assuming conservation of $\bar{\theta}_e$ is shown in the red solid line. Good agreement is observed both when no eccentricity excitation occurs ($I_0 \lesssim 50^\circ$ and $I_0 \gtrsim 130^\circ$) and when $|\mathcal{A}| \gg 1$ ($80^\circ \lesssim I_0 \lesssim 100^\circ$). However, we see in Fig. 11 that for intermediate inclinations $I_0 \in [50, 80]$ and $I_0 \in [100, 130]$, $\theta_{sl,f}$ varies over a large range and does not agree with the prediction of $\bar{\theta}_e$ conservation. This pattern of deviations is different than that seen in the fiducial parameter regime (Fig. 2), as this inclination regime corresponds to neither the fastest nor slowest merging systems.

We attribute the origin of these deviations to resonance interactions. Fig. 12 illustrates that these intermediate inclinations are closer to the $\bar{\Omega}_e = \Omega_{LK}$ resonance than inclinations very close to 90° . In addition, as the inner binary coalesces under GW radiation, e_{min} becomes larger (e.g. see Fig. 1), so the locations of the resonances sweep away from $I = 90^\circ$. As the location of the resonances is a sensitive function of e_{min} , resonance passage is likely nonadiabatic. Thus, we expect that all systems that encounter the resonance,

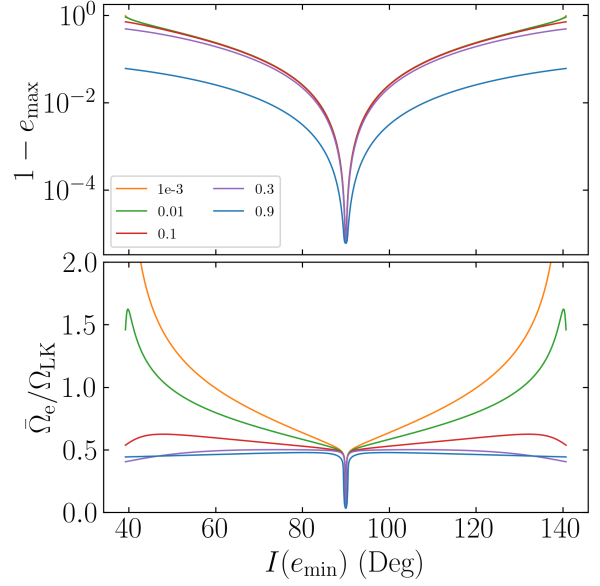


Figure 10. e_{max} and $\bar{\Omega}_e/\Omega_{LK}$ as a function of $I(e_{min})$, the inclination of the inner binary at eccentricity minimum, for varying values of e_{min} (different colors) for the fiducial parameter regime. In the fiducial parameter regime, where only systems with $I_0 \approx 90^\circ$ will merge within a Hubble time, $I(e_{min}) \sim 90^\circ$ for most of the evolution (see Fig. 1) until $e_{min} \approx 1$ is satisfied. This plot then shows that $\bar{\Omega}_e \lesssim 0.5\Omega_{LK}$ is a general feature of LK-induced mergers, as is the case for the fiducial simulation (see Fig. 5).

i.e. all systems with intermediate initial inclinations, will experience an impulsive kick to $\bar{\theta}_e$, resulting in poor $\bar{\theta}_e$ conservation. This result is denoted by the broad red shaded regions in Fig. 11.

For initial inclinations closer to 90° , these systems start at the edge of the $N = 1$ resonance and quickly evolve away from it (as e_{min} increases and causes $\bar{\Omega}_e/\Omega_{LK}$ to decrease), so the cumulative effect of the resonance interaction is well predicted by evaluating Eq. (74) for $N = 1$ at the initial conditions. This is denoted by the narrow red shaded region surrounding the red line near $I_0 = 90^\circ$ in Fig. 11. We see that the scatter is well predicted for these weakly-resonant conditions. We empirically choose the transition between “weakly” and “strongly” resonant systems when the $|\Delta\bar{\theta}_e|$ predicted by Eq. (74) exceeds 6° .

To understand the general characteristics of systems that interact strongly with resonances, we examine the quantities in Eq. (74):

- $\sin(\Delta I_{eN})$ is small unless $\mathcal{A} \simeq 1$. Otherwise, Ω_e does not nutate appreciably within a LK cycle, and all the Ω_{eN} are aligned with $\bar{\Omega}_e$, implying all the $\Delta I_{eN} \approx 0$.
- Smaller values of e_{min} increase $\bar{\Omega}_e/\Omega_{LK}$, as shown in Fig. 12.

However, the timescales over which \mathcal{A} increases and e_{min} decreases are comparable (see Fig. 1). This implies that, if $\mathcal{A} \ll 1$ initially, which is the case for LK-induced mergers, then e_{min} will be very close to unity when \mathcal{A} grows to be $\simeq 1$, and the contribution predicted by Eq. (74) will remain small throughout the entire evolution. On the other hand, only if $\mathcal{A} \approx 1$ and $e_{min} \ll 1$ initially, as is the case for the intermediate inclinations in the LK-enhanced regime, are resonant interactions likely to be significant.

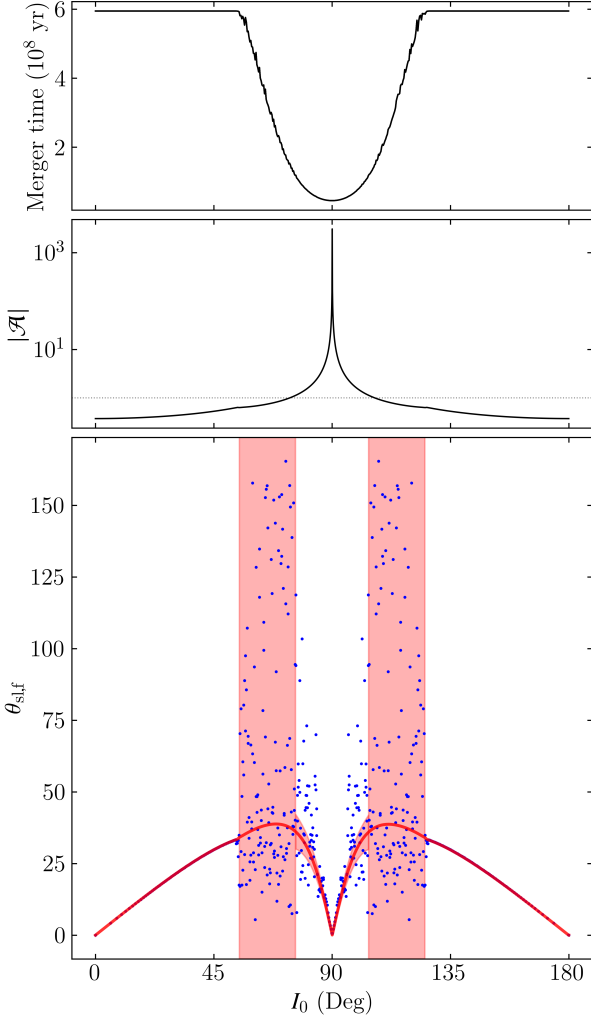


Figure 11. The merger time (top), the magnitude of the adiabaticity parameter $|\mathcal{A}| \equiv \Omega_{\text{SL}}/|\Omega_{\text{L}}|$ (middle), and the final spin-orbit misalignment angle $\theta_{\text{sl},f}$ (bottom) for the LK-enhanced parameter regime, i.e. $m_1 = m_2 = 30M_\odot$, $m_3 = 3 \times 10^7 M_\odot$, $a_0 = 0.1$ AU, $e_0 = 10^{-3}$, $\bar{a}_{\text{out}} = 300$ AU, and $e_{\text{out}} = 0$. In the middle panel, the horizontal dashed line indicates $|\mathcal{A}| = 1$. On the bottom panel, the blue dots denote results from numerical simulations with $\theta_{\text{sl},f} = 0$. The prediction for $\theta_{\text{sl},f}$ assuming conservation of θ_e is shown as the red line, which agrees well with the data both when there is no eccentricity excitation ($I \lesssim 50^\circ$ and $I \gtrsim 130^\circ$) and when $|\mathcal{A}| \gg 1$. The red shaded area shows the predicted deviation from conservation of θ_e , given by Eq. (74) for $N = 1$. For a substantial range of intermediate inclinations ($I \in [50^\circ, 80^\circ]$ and $I \in [100^\circ, 130^\circ]$), the spin is significantly affected the resonances as they sweep away from $I = 90^\circ$ (see Fig. 12). As such, these initial inclinations are expected to have uncorrelated $\theta_{\text{sl},f}$ and $\theta_{e,0}$, and we denote this range with a broad red shaded interval.

6 STELLAR MASS BLACK HOLE TRIPLES

In this section, we extend our predictions for the final spin-orbit misalignment angle $\theta_{\text{sl},f}$ to systems where all three masses are comparable and the ratio of the angular momenta of the two binaries, given by

$$\eta \equiv \frac{L}{L_{\text{out}}} \Big|_{e=e_{\text{out}}=0} = \frac{\mu}{\mu_{\text{out}}} \left[\frac{m_{12}a}{m_{123}a_{\text{out}}} \right]^{1/2}, \quad (75)$$

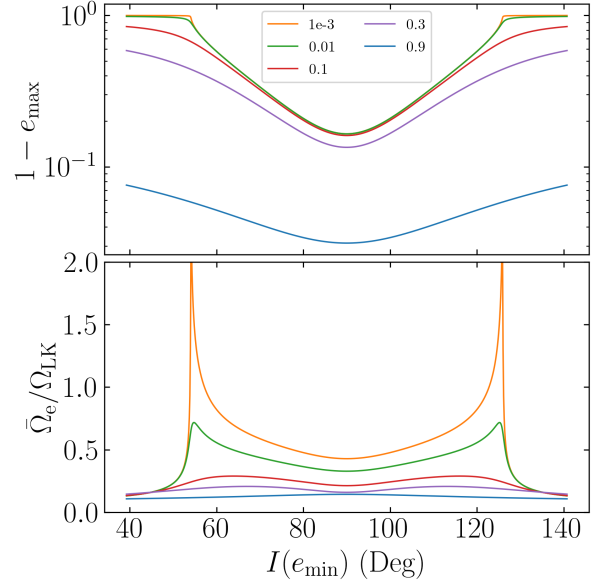


Figure 12. Same as Fig. 10 but for the LK-enhanced parameter regime. In the LK-enhanced regime, all I_0 merge within a Hubble time, and it is clear that $\bar{\Omega}_e \approx \Omega_{\text{LK}}$ can be satisfied for a wide range of inclinations. However, $e_{\text{max}} \lesssim 0.8$ for these inclinations is moderate compared to the LK-induced regime.

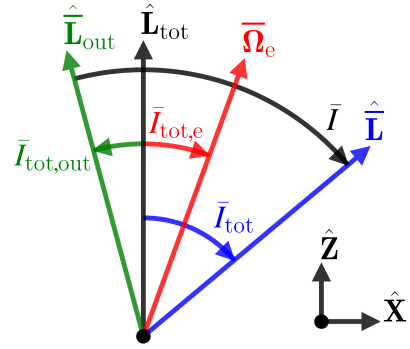


Figure 13. Definition of angles in the case where L/L_{out} is nonzero. Similar to before, we choose the convention where $\bar{I}_{\text{tot,e}} \in [0^\circ, 90^\circ]$ when $\bar{\Omega}_L > 0$ and $\bar{I}_{\text{tot,e}} \in [90^\circ, 180^\circ]$ when $\bar{\Omega}_L < 0$. Here, \mathbf{L}_{out} is not fixed, but $\mathbf{L}_{\text{tot}} \equiv \mathbf{L} + \mathbf{L}_{\text{out}}$ is. Note that the coordinate system is now oriented with $\hat{\mathbf{Z}} \propto \hat{\mathbf{L}}_{\text{tot}}$.

where $m_{123} = m_{12} + m_3$ and $\mu_{\text{out}} = m_{12}m_3/m_{123}$, is not negligible. When $\eta \neq 0$, \mathbf{L}_{out} is no longer fixed, but the total angular momentum $\mathbf{L}_{\text{tot}} \equiv \mathbf{L} + \mathbf{L}_{\text{out}}$ is fixed. We choose the coordinate system with $\hat{\mathbf{Z}} = \hat{\mathbf{L}}_{\text{tot}}$, shown in Fig. 13.

To analyze this system, we still assume $e_{\text{out}} \ll 1$ so that the octupole-order effects are negligible. To calculate the evolution of \mathbf{L} , it is only necessary to evolve a single orbital element for the outer binary, the inclination $I_{\text{tot,out}}$ relative to the total angular momentum, in addition to the orbital elements of the inner binary (a , e , φ , I_{tot} , and ω), as the ascending node of the outer binary satisfies $\varphi_{\text{out}} = \varphi + 180^\circ$. The equations of motion are given by

(Liu et al. 2015)

$$\frac{da}{dt} = \left(\frac{da}{dt} \right)_{\text{GW}}, \quad (76)$$

$$\frac{de}{dt} = \frac{15}{8t_{\text{LK}}} e j(e) \sin 2\omega \sin^2 I + \left(\frac{de}{dt} \right)_{\text{GW}}, \quad (77)$$

$$\frac{d\Omega_L}{dt} = \frac{L_{\text{tot}}}{L_{\text{out}}} \frac{3}{4t_{\text{LK}}} \frac{\cos I (5e^2 \cos^2 \omega - 4e^2 - 1)}{j(e)}, \quad (78)$$

$$\frac{dI_{\text{tot}}}{dt} = -\frac{15}{16t_{\text{LK}}} \frac{e^2 \sin 2\omega \sin 2I}{j(e)}, \quad (79)$$

$$\frac{dI_{\text{tot,out}}}{dt} = -\eta \frac{15}{8t_{\text{LK}}} (e^2 \sin 2\omega \sin I), \quad (80)$$

$$\begin{aligned} \frac{d\omega}{dt} = & \frac{3}{t_{\text{LK}}} \left\{ \frac{4 \cos^2 I + (5 \cos(2\omega) - 1)(1 - e^2 - \cos^2 I)}{8j(e)} \right. \\ & \left. + \frac{\eta \cos I}{8} [2 + e^2(3 - 5 \cos(2\omega))] \right\} + \Omega_{\text{GR}}, \end{aligned} \quad (81)$$

where $I = I_{\text{tot}} + I_{\text{tot,out}}$ is the relative inclination between the two angular momenta. The spin evolution of one of the inner BHs is then described in the corotating with \mathbf{L} about \mathbf{L}_{tot} by the equation of motion

$$\left(\frac{d\mathbf{S}}{dt} \right)_{\text{rot}} = \Omega_e \times \mathbf{S}, \quad (82)$$

where

$$\begin{aligned} \Omega_e &\equiv \Omega_{\text{SL}} \hat{\mathbf{L}} + \Omega_L \hat{\mathbf{L}}_{\text{tot}}, \\ &= \overline{\Omega_{\text{SL}} \sin I_{\text{tot}}} \hat{\mathbf{X}} + (\overline{\Omega_L} + \overline{\Omega_{\text{SL}} \cos I_{\text{tot}}}) \hat{\mathbf{Z}}, \end{aligned} \quad (83)$$

where $\Omega_L = -d\Omega_L/dt$ [Eq. (78)] is the rate of precession of \mathbf{L} about \mathbf{L}_{tot} , and bars denote averaging over an LK cycle. We define the averaged quantities

$$\overline{\Omega_{\text{SL}} \sin I_{\text{out}}} \equiv \overline{\Omega_{\text{SL}} \sin \bar{I}_{\text{out}}}, \quad \overline{\Omega_{\text{SL}} \cos I_{\text{out}}} \equiv \overline{\Omega_{\text{SL}} \cos \bar{I}_{\text{out}}}. \quad (84)$$

The results of Section 4 suggest that the angle $\bar{\theta}_e$ is an adiabatic invariant, where $\bar{\theta}_e$ is given by

$$\cos \bar{\theta}_e \equiv \frac{\overline{\Omega_e}}{\overline{\Omega_e}} \cdot \bar{\mathbf{S}}, \quad (85)$$

where $\bar{\mathbf{S}}$ is the spin vector averaged over a LK cycle. The orientation of $\overline{\Omega_e}$ is described by the inclination angle $\bar{I}_{\text{tot,e}}$ (Fig. 13), which can be expressed using Eq. (83)

$$\tan \bar{I}_{\text{tot,e}} = \frac{\mathcal{A} \sin \bar{I}_{\text{tot}}}{1 + \mathcal{A} \cos \bar{I}_{\text{tot}}}, \quad (86)$$

where $\mathcal{A} \equiv \overline{\Omega_{\text{SL}}}/\overline{\Omega_L}$ is the adiabaticity parameter.

At $t = t_f$, the inner binary is sufficiently compact that θ_{sl} is frozen (see bottom right panel of Fig. 1), and the system satisfies $\mathcal{A} \gg 1$ ($\overline{\Omega_{\text{SL}}} \propto a^{-5/2}$ while $\overline{\Omega_L} \propto a^{3/2}$). When this is satisfied, $\overline{\Omega_e} \parallel \mathbf{L}$, and so $\bar{\theta}_{e,f} = \theta_{\text{sl},f}$. Then, since adiabatic invariance implies $\bar{\theta}_{e,f} = \bar{\theta}_{e,0}$,

$$\theta_{\text{sl},f} = \bar{\theta}_{e,0}. \quad (87)$$

First, we consider the case where $\mathbf{S}_0 = \hat{\mathbf{L}}_0$. Then $\bar{\theta}_{e,0} = |I_{\text{tot},0} - \bar{I}_{\text{tot,e},0}|$ (see Fig. 13), and so

$$\theta_{\text{sl},f} = |I_{\text{tot},0} - \bar{I}_{e,0}|. \quad (88)$$

Suppose additionally that the binary initially satisfies $|\overline{\Omega_L}| \gg \overline{\Omega_{\text{SL}}}$, then $\overline{\Omega_e}$ is either parallel or anti-parallel to \mathbf{L}_{tot} depending on

whether $\overline{\Omega_L}$ is positive or negative. Define I_c to be the starting mutual inclination for which $\overline{\Omega_L}$ changes sign. Note that $I_c > 90^\circ$: even though Ω_L changes sign at 90° , the inclination decreases over a LK cycle for $I < I_{\text{lim}}$ (where $I_{\text{lim}} > 90^\circ$ is the starting mutual inclination that maximizes e_{max} (Liu & Lai 2018)), so the sign of $\overline{\Omega_L}$ changes over a LK cycle when $90^\circ < I_0 < I_{\text{lim}}$. We find that

$$\theta_{\text{sl},f} = \begin{cases} I_{\text{tot},0} & I_0 < I_c, \\ 180^\circ - I_{\text{tot},0} & I_0 > I_c. \end{cases} \quad (89)$$

More generally, so long as $\mathcal{A} \ll 1$ initially, we can specify the initial spin orientation by $\theta_{s,\text{tot},0}$, the initial angle between \mathbf{S} and \mathbf{L}_{tot} , giving

$$\theta_{\text{sl},f} = \begin{cases} \theta_{s,\text{tot},0} & I < I_c, \\ 180^\circ - \theta_{s,\text{tot},0} & I > I_c. \end{cases} \quad (90)$$

We first compare these results to numerical simulations by considering a stellar-mass BH triple that is in the LK-induced regime: we use the same inner binary parameters as the fiducial system before, but use a tertiary companion with $m_3 = 30M_\odot$, $a_{\text{out}} = 4500$ AU, and $e_{\text{out}} = 0$. Fig. 14 shows that Eq. (88) accurately predicts $\theta_{\text{sl},f}$ when $\theta_{\text{sl},0} = 0^\circ$ for this parameter regime when conservation of $\bar{\theta}_e$ is good. Furthermore, deviations from exact $\bar{\theta}_e$ conservation are well described by Eq. (60), the prediction of the theory in Section 4. Unlike the $\eta = 0$ case (Fig. 2), $\theta_{\text{sl},f}$ is not symmetric about $I_c \approx 92.14^\circ$. This is because $|\Omega_L|$ is not exactly equal on either side of I_c . Additionally, unlike in the $\eta = 0$ case, the minimum $\theta_{\text{sl},f}$ is not exactly zero. We showed in Section 4.4 that when $\eta = 0$, \mathbf{L} is fixed when $I_0 = 90^\circ$, as $d\Omega_L/dt = dI/dt = 0$. For nonzero η , $d\Omega_L/dt$ and dI_{tot}/dt are not zero at $I_0 = I_c$.

Eq. (88) also gives good agreement LK-enhanced merger regime. We consider the same inner binary parameters as in Section 5.4 but use a tertiary companion with $m_3 = 30M_\odot$, $a_{\text{out}} = 3$ AU, and $e_{\text{out}} = 0$. The results are shown in Fig. 15.

7 CONCLUSION AND DISCUSSION

In this paper, we consider the evolution of the final spin-orbit misalignment angle θ_{sl} of LK-induced binary BH mergers. We study cases where the tertiary companion is either a supermassive black hole (SMBH) or a stellar mass black hole (BH). We show that, when the tertiary orbit is circular and octupole effects are unimportant, the spin vectors of the inner BHs obey the simple equation of motion Eq. (21). Analysis of this equation yields the following conclusions:

- For most parameters of astrophysical relevance, the angle $\bar{\theta}_e$ [Eq. (35)] is an adiabatic invariant. Since the inner BH binary merges in finite time, $\bar{\theta}_e$ is only conserved to finite accuracy; we show that the deviation from perfect adiabaticity can be predicted from initial conditions [see Eq. 51 and Fig. 9].
- When the resonant condition $\bar{\Omega_e} \approx N\Omega_{\text{LK}}$ for integer N is satisfied, significant oscillations in $\bar{\theta}_e$ can arise. We derive an analytic estimate of this oscillation amplitude [Eq. (74)]. This estimate both demonstrates that the resonance is unimportant for “LK-induced” mergers and qualitatively explains the scatter in $\theta_{\text{sl},f}$ seen by LL17 (see Fig. 11).

In previous work, LL18 found that the final spin-orbit misalignment angle $\theta_{\text{sl},f}$ exhibits a 90° attractor (Fig. 2) when the octupole effect is negligible. Our theory shows that this attractor is a result of their taking $\theta_{\text{sl},0} = 0^\circ$ (in agreement with Yu et al. 2020), as

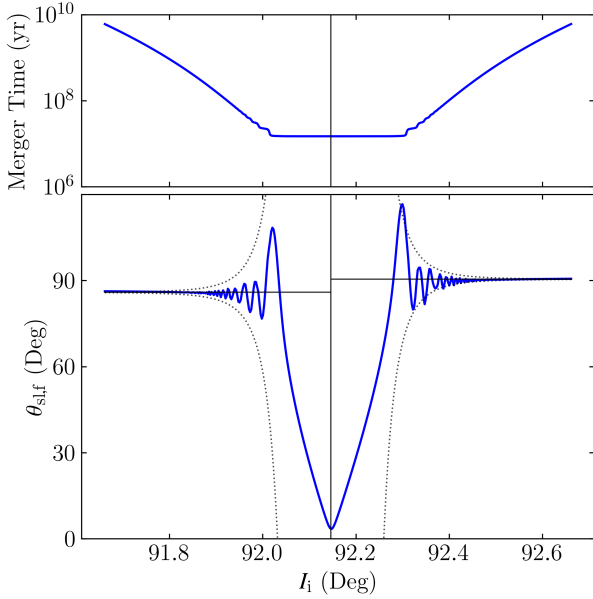


Figure 14. Similar to Fig. 2 but for stellar-mass tertiary $m_3 = 30M_\odot$ and $\bar{a}_3 = 4500$ AU. The vertical black line denotes $I_c \approx 92.14^\circ$, the inclination for which Ω_L changes signs, and the two horizontal lines denote the predictions of Eq. (88). The dotted black lines bound the deviation due to non-adiabatic evolution, given by Eq. (60).

the initial and final spin orientations are related via conservation of $\bar{\theta}_e$ (Sections 4.4 and 6). Note that the component BH spins in the recent LIGO detection GW190521 have spin-orbit misalignment angle $\sim 90^\circ$ (Abbott et al. 2020). If the evolution history of the component BHs resembled our LK-induced scenario, a primordial $\theta_{sl,0} \approx 0^\circ$ would be consistent with the observed outcome.

The systems detected by LIGO in O1 and O2 have $\chi_{\text{eff}} \approx 0$, where χ_{eff} is given by Eq. (1) (e.g. Abbott et al. 2016, 2019). One possible explanation for this is that BHs are born slowly rotating (e.g. Fuller & Ma 2019). Our mechanism provides an alternative origin for this behavior with no assumptions on the BH spin magnitudes if $\theta_{sl,0} \approx 0^\circ$. We also quantify the expected scatter from the perfect 90° attractor reported by LL18 due to either non-adiabaticity or resonances during the inspiral.

When the tertiary orbit is eccentric, the octupole-order contributions can no longer be neglected. The octupole-order LK effect is not integrable, and the eccentricity excitations are no longer regular (see e.g. Liu & Lai 2018). In this case, Ω_e has neither consistent direction nor magnitude, and our theory cannot be applied. In fact, the resulting $\theta_{sl,f}$ distribution is largely unrelated to the initial $\bar{\theta}_{e,0}$ (Liu & Lai 2018).

If the system is not sufficiently hierarchical (a_{out} is too small), the double averaging approximation breaks down, and the dynamics are no longer integrable, so there is little reason to expect any relation between $\theta_{sl,f}$ and $\bar{\theta}_{e,0}$. However, Liu & Lai (2018) found that the double averaged equations predict the correct merger window and merger fractions even beyond their regime of validity if the octupole effect is weak, so it is possible that our results concerning $\theta_{sl,f}$ are also somewhat robust even when the double averaged equations formally break down. We defer this possibility to future work.

Finally, in this work, we only follow the evolution of θ_{sl} until the orbital separation is ≤ 0.5 AU for the LK-induced mergers, and

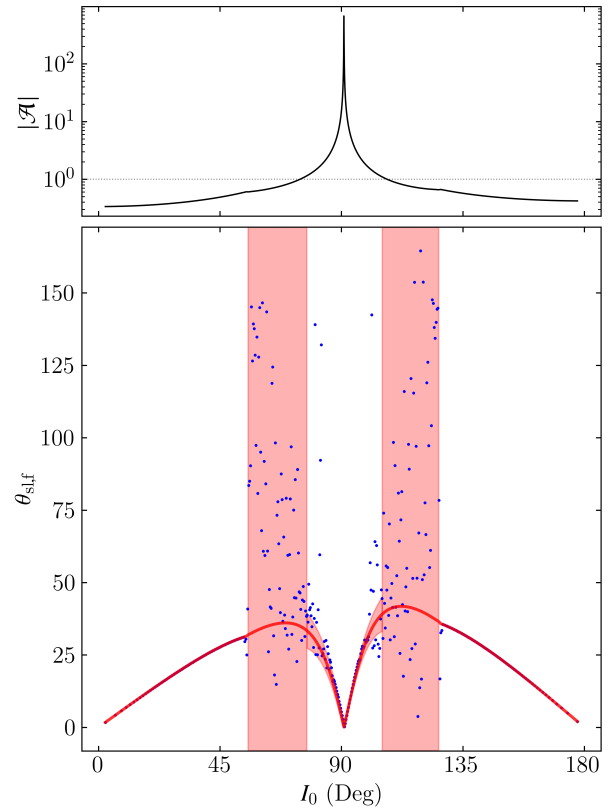


Figure 15. Similar to Fig. 11 except with stellar mass tertiary $m_3 = 30M_\odot$ and $\bar{a}_{\text{out}} = 3$ AU.

≤ 0.1 AU for the LK-enhanced mergers. To leading post-Newtonian (PN) order, θ_{sl} is constant for separations smaller than these until the spin-spin interaction (2 PN) becomes important [Eq. (19)]. This interaction is negligible until the binary enters the LIGO band (Liu et al. 2019; Yu et al. 2020).

REFERENCES

- Abbott B., et al., 2016, *Phys. Rev. Lett.*, 116, 061102
- Abbott B., et al., 2019, *The Astrophysical Journal Letters*, 882, L24
- Abbott R., et al., 2020, *The Astrophysical Journal Letters*, 900, L13
- Anderson K. R., Storch N. I., Lai D., 2016, *Monthly Notices of the Royal Astronomical Society*, 456, 3671
- Antonini F., Perets H. B., 2012, *The Astrophysical Journal*, 757, 27
- Antonini F., Toonen S., Hamers A. S., 2017, *The Astrophysical Journal*, 841, 77
- Antonini F., Rodriguez C. L., Petrovich C., Fischer C. L., 2018, *Monthly Notices of the Royal Astronomical Society: Letters*, 480, L58
- Banerjee S., Baumgardt H., Kroupa P., 2010, *Monthly Notices of the Royal Astronomical Society*, 402, 371
- Belczynski K., Dominik M., Bulik T., O’Shaughnessy R., Fryer C., Holz D. E., 2010, *The Astrophysical Journal Letters*, 715, L138
- Belczynski K., Holz D. E., Bulik T., O’Shaughnessy R., 2016, *Nature*, 534, 512
- Belczynski K., et al., 2020, *Astronomy & Astrophysics*, 636, A104
- Blaes O., Lee M. H., Socrates A., 2002, *The Astrophysical Journal*, 578, 775
- Chicone C., 2006, *Ordinary differential equations with applications*. Vol. 34, Springer Science & Business Media

- Dominik M., Belczynski K., Fryer C., Holz D. E., Berti E., Bulik T., Mandel I., O'Shaughnessy R., 2012, *The Astrophysical Journal*, 759, 52
- Dominik M., Belczynski K., Fryer C., Holz D. E., Berti E., Bulik T., Mandel I., O'Shaughnessy R., 2013, *The Astrophysical Journal*, 779, 72
- Dominik M., et al., 2015, *The Astrophysical Journal*, 806, 263
- Downing J., Benacquista M., Giersz M., Spurzem R., 2010, *Monthly Notices of the Royal Astronomical Society*, 407, 1946
- Floquet G., 1883, in *Annales scientifiques de l'École normale supérieure*. pp 47–88
- Fuller J., Ma L., 2019, *The Astrophysical Journal Letters*, 881, L1
- Gondán L., Kocsis B., Raffai P., Frei Z., 2018, *The Astrophysical Journal*, 860, 5
- Hoang B.-M., Naoz S., Kocsis B., Rasio F. A., Dosopoulou F., 2018, *The Astrophysical Journal*, 856, 140
- Kinoshita H., 1993, *Celestial Mechanics and Dynamical Astronomy*, 57, 359
- Lipunov V., Postnov K., Prokhorov M., 1997, *Astronomy Letters*, 23, 492
- Lipunov V., et al., 2017, *Monthly Notices of the Royal Astronomical Society*, 465, 3656
- Liu B., Lai D., 2017, *The Astrophysical Journal Letters*, 846, L11
- Liu B., Lai D., 2018, *The Astrophysical Journal*, 863, 68
- Liu B., Muñoz D. J., Lai D., 2015, *Monthly Notices of the Royal Astronomical Society*, 447, 747
- Liu B., Lai D., Wang Y.-H., 2019, *The Astrophysical Journal*, 881, 41
- Magnus W., 1954, *Communications on pure and applied mathematics*, 7, 649
- Miller M. C., Hamilton D. P., 2002, *The Astrophysical Journal*, 576, 894
- Miller M. C., Lauburg V. M., 2009, *The Astrophysical Journal*, 692, 917
- O'leary R. M., Rasio F. A., Fregeau J. M., Ivanova N., O'Shaughnessy R., 2006, *The Astrophysical Journal*, 637, 937
- Podsiadlowski P., Rappaport S., Han Z., 2003, *Monthly Notices of the Royal Astronomical Society*, 341, 385
- Postnov K., Kuranov A., 2019, *Monthly Notices of the Royal Astronomical Society*, 483, 3288
- Randall L., Xianyu Z.-Z., 2018, *The Astrophysical Journal*, 853, 93
- Rodriguez C. L., Morscher M., Pattabiraman B., Chatterjee S., Haster C.-J., Rasio F. A., 2015, *Physical Review Letters*, 115, 051101
- Rodriguez C. L., Amaro-Seoane P., Chatterjee S., Rasio F. A., 2018, *Physical Review Letters*, 120, 151101
- Samsing J., D'Orazio D. J., 2018, *Monthly Notices of the Royal Astronomical Society*, 481, 5445
- Samsing J., Ramirez-Ruiz E., 2017, *The Astrophysical Journal Letters*, 840, L14
- Schmidt P., Ohme F., Hannam M., 2015, *Physical Review D*, 91, 024043
- Silsbee K., Tremaine S., 2016, arXiv preprint arXiv:1608.07642
- Storch N. I., Lai D., 2015, *Monthly Notices of the Royal Astronomical Society*, 448, 1821
- Storch N. I., Anderson K. R., Lai D., 2014, *Science*, 345, 1317
- Storch N. I., Lai D., Anderson K. R., 2017, *Monthly Notices of the Royal Astronomical Society*, 465, 3927
- Wen L., 2003, *The Astrophysical Journal*, 598, 419
- Yu H., Ma S., Giesler M., Chen Y., 2020, arXiv preprint arXiv:2007.12978
- Ziosi B. M., Mapelli M., Branchesi M., Tormen G., 2014, *Monthly Notices of the Royal Astronomical Society*, 441, 3703
- Zwart S. F. P., McMillan S. L., 1999, *The Astrophysical Journal Letters*, 528, L17
- Zwillinger D., 2002, *CRC standard mathematical tables and formulae*. CRC press

APPENDIX A: FLOQUET THEORY ANALYSIS

In this appendix, we provide an alternative approach to analyzing the BH spin dynamics based on Floquet theory (Chicone 2006) that provides results complementary to those in the main text. Though the resulting equations cannot be analytically solved, they place strong constraints on the allowed behavior of the system. Additionally, Eq. (??) finds a natural interpretation in this formulation, and its accuracy is numerically tested in Appendix A3. We again work in the corotating frame and neglect GW dissipation, so the equation of motion is given by Eq. (21). If we define the matrix operator satisfying $\tilde{\mathbf{A}}\mathbf{S} = \Omega_e \times \mathbf{S}$, then the equation of motion is

$$\left(\frac{d\mathbf{S}}{dt}\right)_{\text{rot}} = \tilde{\mathbf{A}}\mathbf{S}. \quad (\text{A1})$$

Here, $\tilde{\mathbf{A}}$ is periodic with period T_{LK} .

A1 Without Nutation

First, for simplicity, let us assume that Ω_e does not nutate, so its orientation is fixed. In this case, Eq. (A1) admits an exact conserved quantity:

$$\frac{d}{dt} \left[e^{-\Phi} \mathbf{S} \right] = 0, \quad (\text{A2})$$

where

$$\Phi(t) \equiv \int_0^t \tilde{\mathbf{A}} dt. \quad (\text{A3})$$

Separately, since Eq. (A1) is linear and has periodic coefficients, Floquet theory tells us that $\mathbf{S}(t + T_{\text{LK}})$ is related to $\mathbf{S}(t)$ by the monodromy matrix $\tilde{\mathbf{M}}$:

$$\mathbf{S}(t + T_{\text{LK}}) = \tilde{\mathbf{M}}\mathbf{S}(t). \quad (\text{A4})$$

Comparing Eqs. (A2) and (A4), we immediately find that

$$\begin{aligned} \tilde{\mathbf{M}} &= \exp \left[\int_0^{T_{\text{LK}}} \tilde{\mathbf{A}} dt \right], \\ &= \exp \left[T_{\text{LK}} \tilde{\mathbf{A}} \right], \end{aligned} \quad (\text{A5})$$

where again the overline denotes time averaging. As $\tilde{\mathbf{M}}$ is a rotation matrix, call \mathbf{R} its rotation axis, or its eigenvector with eigenvalue 1. But $\mathbf{R} = \hat{\Omega}_e$, so $\mathbf{S} \cdot \hat{\Omega}_e$ must be constant for every $t = NT_{\text{LK}}$.

This example is somewhat trivial, as if Ω_e does not nutate, then \mathbf{S} just precesses around fixed $\mathbf{R} = \hat{\Omega}_e$ at a variable rate, and $\mathbf{S} \cdot \hat{\Omega}_e$ is conserved. However, the equation of motion studied in Section 4 [Eq. (34)] neglects nutation yet provides a good description of the evolution of $\bar{\theta}_e$. For the fiducial LK-induced merger, Fig. 6 shows that Ω_e nutates substantially within a LK period when $\mathcal{A} \simeq 1$ (nutation is equivalent to $\Omega_{e1} \neq 0$ and $\Delta I_{e1} \neq 0^\circ$). We infer that, even when Ω_e does nutate appreciably, there are conditions for which its nutation negligibly affects $\bar{\theta}_e$ conservation.

In the main text, Section 5 showed that being close to a resonance $\bar{\Omega}_e \approx N\Omega_{\text{LK}}$ results in non-conservation of $\bar{\theta}_e$. However, the converse is not obviously true: our approximate analysis does not prove that being far from these resonances guarantees good conservation of $\bar{\theta}_e$. In the next section, we argue that, for the dynamics studied in this paper, this converse is likely true as well.

A2 With Nutation

When Ω_e is allowed to nutate within T_{LK} , the quantity given by Eq. (A2) is no longer conserved, as

$$\frac{d}{dt} \left[e^{-\Phi} \mathbf{S} \right] = e^{-\Phi} \frac{d\mathbf{S}}{dt} - \tilde{\mathbf{A}} e^{-\Phi} \mathbf{S} \neq e^{-\Phi} \left[\frac{d\mathbf{S}}{dt} - \tilde{\mathbf{A}} \mathbf{S} \right] = 0. \quad (\text{A6})$$

Instead, we define new quantities Φ' and $\tilde{\mathbf{B}}$ defined such that

$$\Phi'(t) \equiv \int_0^t \tilde{\mathbf{A}} + \tilde{\mathbf{B}} dt, \quad (\text{A7})$$

$$\frac{d}{dt} \left[e^{-\Phi'} \mathbf{S} \right] = 0. \quad (\text{A8})$$

This requires

$$\tilde{\mathbf{B}} = \left[e^{-\Phi'}, \tilde{\mathbf{A}} \right] e^{\Phi'}, \quad (\text{A9})$$

where the square brackets denote the commutator. The monodromy matrix is then

$$\tilde{\mathbf{M}} = \exp \left[\int_0^{T_{\text{LK}}} \tilde{\mathbf{A}} + \tilde{\mathbf{B}} dt \right]. \quad (\text{A10})$$

We next want to understand when Eq. (A10) can be well approximated by Eq. (A5). We first expand the matrix exponential using the Zassenhaus formula (the inverse of the well-known Baker-Campbell-Hausdorff formula, see e.g. Magnus 1954)

$$\tilde{\mathbf{M}} = e^{T_{\text{LK}} \tilde{\mathbf{A}}} e^{T_{\text{LK}} \tilde{\mathbf{B}}} \exp \left[-\frac{T_{\text{LK}}^2 [\tilde{\mathbf{A}}, \tilde{\mathbf{B}}]}{2} + \dots \right]. \quad (\text{A11})$$

Note that $\tilde{\mathbf{M}}$ is a rotation matrix (see Section 3.1), and $\exp \left[T_{\text{LK}} \tilde{\mathbf{A}} \right]$ is also a rotation matrix ($\tilde{\mathbf{A}}$ is skew-symmetric), so the remainder of the right hand side above must also be a rotation matrix (as the rotation matrices are closed under matrix multiplication). For convenience, define

$$\tilde{\mathbf{R}}_A \equiv e^{T_{\text{LK}} \tilde{\mathbf{A}}} \quad \tilde{\mathbf{R}}_B \equiv e^{T_{\text{LK}} \tilde{\mathbf{B}}} \exp \left[-\frac{T_{\text{LK}}^2 [\tilde{\mathbf{A}}, \tilde{\mathbf{B}}]}{2} + \dots \right], \quad (\text{A12})$$

where $\tilde{\mathbf{R}}_A$ and $\tilde{\mathbf{R}}_B$ are rotation matrices that effect rotations by angles θ_A and θ_B about their respective axes.

When can $\tilde{\mathbf{R}}_B$ be neglected? From Eq. (A9), we see that $\tilde{\mathbf{B}} = 0$ vanishes ($\theta_B = 0$) when $[\tilde{\mathbf{A}}, \Phi]$ commute, which occurs when Ω_e does not nutate, and we recover Eq. (A5). In fact, we will argue later that θ_B is generally small for the spin dynamics studied in the main text. However, a small θ_B alone is not sufficient to assume $\tilde{\mathbf{M}} \approx \tilde{\mathbf{R}}_A$. To see this, note if θ_B is small, then $\tilde{\mathbf{R}}_B \approx \mathbf{1}$ where $\mathbf{1}$ is the 3×3 identity matrix. On the other hand, $\theta_A = \bar{\Omega}_e T_{\text{LK}}$. Then, if θ_A is not too near an integer multiple of 2π , $\tilde{\mathbf{M}} \approx \tilde{\mathbf{R}}_A$ and $\tilde{\mathbf{M}} \approx \tilde{\mathbf{R}}_A$ as before. However, if $\bar{\Omega}_e T_{\text{LK}} \approx 2\pi N$ for integer N , then $\tilde{\mathbf{R}}_A$ itself is near the identity as well, and $\tilde{\mathbf{R}}_B$ cannot be neglected when calculating $\tilde{\mathbf{M}}$. The criterion for neglecting $\tilde{\mathbf{R}}_B$ is then clear: θ_B must be much closer to $2\pi N$ for integer N than θ_A .

To complete this picture, we argue that, for the spin dynamics studied in the main text, θ_B is small, so generally $\tilde{\mathbf{R}}_B \approx \mathbf{1}$, and $\bar{\Omega}_e \approx N\Omega_{\text{LK}}$ is a *necessary* condition for \mathbf{R} to differ significantly from $\hat{\Omega}_e$. To do this, we recall that $\bar{\Omega}_e T_{\text{LK}} \lesssim 2\pi$ (Figs. 10 and 12), and we seek to show that θ_B must generally be small compared to θ_A , which would imply $\theta_B \ll 2\pi$. We first approximate that

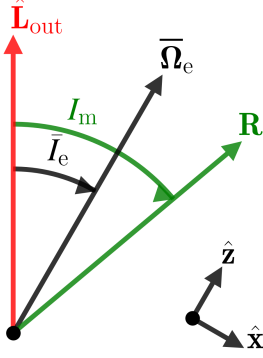


Figure A1. Definition of angles for numerical study of the monodromy matrix rotation axis. \mathbf{R} is the eigenvector of the monodromy matrix $\tilde{\mathbf{M}}$ with eigenvalue 1.

$e^{\Phi'} \approx e^{\Phi}$ in Eq. (A9) (requiring $\theta_B \ll \theta_A$, which we will verify retroactively, and being far from resonance, $\theta_A \neq 2\pi$), which gives

$$\tilde{\mathbf{B}} \approx \left[e^{-\Phi}, \hat{\mathbf{A}} \right] e^{\Phi}. \quad (\text{A13})$$

Next, recall that Φ is the integral of $-\hat{\mathbf{A}}$, and so the magnitude of $\tilde{\mathbf{B}}$ [$\tilde{\mathbf{B}}$ primarily affects $\tilde{\mathbf{M}}$ via its average, see Eq. (A10)] depends on the average misalignment between the vectors Ω_e and $\int^t \Omega_e dt \approx \bar{\Omega}_e$. There are a few possible regimes to consider: (i) if $\mathcal{A} \gg 1$, then LK oscillations are frozen, and Ω_e does not nutate; (ii) if $\mathcal{A} \ll 1$, then $\hat{\Omega}_e \approx \hat{\mathbf{L}}_{\text{tot}} \approx \hat{\bar{\Omega}}_e$ for almost all of T_{LK} ; and (iii) if $\mathcal{A} \simeq 1$, then e_{max} cannot be too large [Eq. (17)], and so Ω_L and Ω_{SL} cannot vary too much within an LK cycle and the nutation of Ω_e is limited. This analysis suggests that, at least far from resonance, the nutation of Ω_e is limited, and the commutator in Eq. (A13) is small in the sense that $\theta_B \ll \theta_A$, justifying our earlier claim. While this analysis is not rigorous, it suggests that the only resonances present in the system are near $\bar{\Omega}_e = N\Omega_{\text{LK}}$, as claimed in the main text, and that otherwise $\mathbf{R} \parallel \bar{\Omega}_e$.

A3 Quantitative Effect

Above, we have given a qualitative analysis of the exact solution for the monodromy matrix $\tilde{\mathbf{M}}$. In this section, we aim to reconcile this with the quantitative, approximate results in the text and suggest that the results in the text constitute a complete characterization of the spin dynamics.

In Section 5, we found that one effect of the $N \geq 1$ Fourier harmonics are fluctuations in $\bar{\theta}_e$ when $\bar{\Omega}_e \approx N\Omega_{\text{LK}}$ with amplitude given by Eq. (74). On the other hand, in Appendix A2, we found that \mathbf{R} is aligned with $\bar{\Omega}_e$ except when $\bar{\Omega}_e$ is sufficiently close to $N\Omega_{\text{LK}}$ that nutation of Ω_e becomes important, but we were not able to determine a closed-form criterion for the misalignment. In this section, we show numerically that the formulas given in the main text give good predictions for the orientation of \mathbf{R} .

To validate the analytic prediction given by Eq. (74), we numerically compute $\tilde{\mathbf{M}}$. We study the $\eta \neq 0$, LK-enhanced regime ($m_1 = m_2 = m_3 = 30M_\odot$, $a_0 = 0.1$ AU, $e_0 = 10^{-3}$, $\tilde{a}_{\text{out}} = 3$ AU). We still neglect GW dissipation in order for Floquet analysis to be applicable. For 2000 different initial inclinations of the inner binary, we construct $\tilde{\mathbf{M}}$ by evolving the spin equation of motion Eq. (21) starting with the three initial conditions $\mathbf{S} = \hat{\mathbf{x}}$, $\mathbf{S} = \hat{\mathbf{y}}$, and $\mathbf{S} = \mathbf{z}$

(see Fig. A1) over a single LK period, then using

$$\tilde{\mathbf{M}} = \Phi(T_{\text{LK}}) \Phi^{-1}(0) = \Phi(T_{\text{LK}}), \quad (\text{A14})$$

where $\Phi(t)$ is the *principal fundamental matrix solution* whose columns are solutions to Eq. (21) and $\Phi(0)$ is the identity. \mathbf{R} is then the eigenvector that has eigenvalue 1. Note that if \mathbf{v} is an eigenvector, so too is $-\mathbf{v}$; we choose convention that \mathbf{R} points in the same direction as $\bar{\Omega}_e$, i.e. $\Delta I_m \equiv |I_m - \bar{I}_e| < 90^\circ$.

The orientation of \mathbf{R} is related to the $|\Delta\bar{\theta}_e|$ predicted by Eq. (74): if \mathbf{R} and $\bar{\Omega}_e$ are misaligned by angle ΔI_m , then $\bar{\theta}_e$ oscillates with semi-amplitude ΔI_m . Thus, we can infer ΔI_m in the vicinity of each $\bar{\Omega}_e = N\Omega_{\text{LK}}$ resonance from Eq. (74). If the total ΔI_m is well approximated by the sum of the contribution from each N harmonic, then we have

$$\Delta I_m \sim \sum_{N=1}^{\infty} \frac{h(N)}{2} \left| \frac{\sin \Delta I_{eN} \Omega_{eN}}{\bar{\Omega}_e - N\Omega_{\text{LK}}} \right|. \quad (\text{A15})$$

Fig. A2 shows that this calculation predicts the numeric ΔI_m well. This supports our assertion that \mathbf{R} deviates from $\bar{\Omega}_e$ at resonances $\bar{\Omega}_e \approx N\Omega_{\text{LK}}$, and the misalignment is captured by Eq. (74).

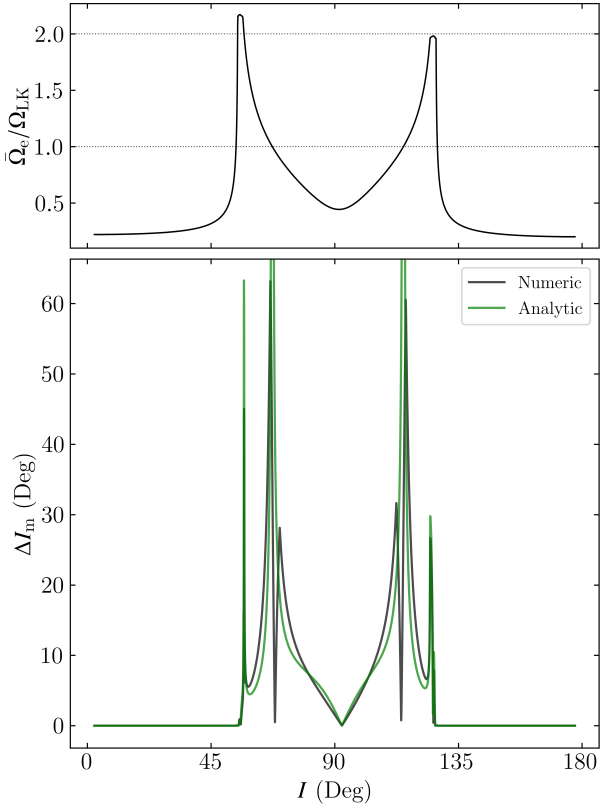


Figure A2. Comparison of the orientation \mathbf{R} obtained from numerical simulations of Eq. (21) in the $\eta \neq 0$, LK-enhanced parameter regime ($m_1 = m_2 = m_3 = 30M_\odot$, $a_0 = 0.1$ AU, $e_0 = 10^{-3}$, $\tilde{a}_{\text{out}} = 3$ AU) with the analytic resonance formula given by Eq. (A15) as a function of initial inclination, in the absence of GW dissipation. The top panel shows the ratio $\bar{\Omega}_e / \Omega_{LK}$ is shown as the solid black line, while the horizontal dashed lines denote $\bar{\Omega}_e = \Omega_{LK}$ and $\bar{\Omega}_e = 2\Omega_{LK}$. The bottom panel shows the misalignment angle between the numerically-computed \mathbf{R} and $\bar{\Omega}_e$ as the black line. Separately, the predicted misalignment ΔI_m due to interaction with the Fourier harmonics is given by Eq. (A15). We see that the scaling of the misalignment angle near resonances is well captured by our analytic formula, but the numerical misalignment angle crosses 0 within the $N = 1$ resonance, which is not predicted by our simple theory.